01 Jan 2023

Microcrystalline Dolomite in a Middle Permian Volcanic Lake: Insights on Primary Dolomite Formation in a Non-Evaporitic Environment

Xin Jiao

Yi Qun Liu

Wan Yang
Missouri University of Science and Technology, yangwa@mst.edu

Hong Li

et. al. For a complete list of authors, see https://scholarsmine.mst.edu/geosci_geo_peteng_facwork/2032

Recommended Citation

X. Jiao et al., "Microcrystalline Dolomite in a Middle Permian Volcanic Lake: Insights on Primary Dolomite Formation in a Non-Evaporitic Environment," *Sedimentology*, vol. 70, no. 1, pp. 48 - 77, Wiley, Jan 2023.
The definitive version is available at https://doi.org/10.1111/sed.13031

SEDIMENTOLOGY the journal of the International Association of Sedimentologists

Sedimentology (2023) **70**, 48–77 doi: 10.1111/sed.13031

Microcrystalline dolomite in a middle Permian volcanic lake: Insights on primary dolomite formation in a non-evaporitic environment

XIN JIAO*, YI-QUN LIU*, WAN YANG†, HONG LI*, ZI-YUAN MENG*, MIN-RU ZHAO* and ZHE-XUAN LI*

**State Key Laboratory of Continental Dynamics, Department of Geology, Northwest University, Xi'an 710069, Shaanxi, China (E-mail: jxin807@163.com)*

†Geology and Geophysics Program, Missouri University of Science and Technology, Rolla, Missouri 65409, USA (E-mail: yangwa@mst.edu)

Associate Editor – Cathy Hollis

ABSTRACT

Lacustrine dolomite nucleation commonly occurs in modern and Neogene evaporitic alkaline lakes. As a result, ancient lacustrine microcrystalline dolomite has been conventionally interpreted to be formed in evaporitic environments. This study, however, suggests a non-evaporitic origin of dolomite precipitated in a volcanic–hydrothermal lake, where hydrothermal and volcanic processes interacted. The dolomite occurs in lacustrine fine-grained sedimentary rocks in the middle Permian Lucaogou Formation in the Santanghu intracontinental rift basin, north-west China. Dolostones are composed mainly of nano-sized to micron-sized dolomite with a euhedral to subhedral shape and a low degree of cation ordering, and are interlaminated and intercalated with tuffaceous shale. Non-dolomite minerals, including quartz, alkaline feldspars, smectite and magnesite mix with the dolomite in various proportions. The $^{87}Sr/^{86}Sr$ ratios (0.704528 to 0.705372, average = 0.705004) and $\delta^{26}Mg$ values (−0.89 to −0.24‰, average = −0.55‰) of dolostones are similar to those of mantle rocks, indicating that the precipitates mainly originated from fluids that migrated upward from the mantle and were subject to water–rock reactions at a great depth. The $\delta^{18}O$ values (−3.1 to −22.7‰, average = −14.0‰) of the dolostones indicate hydrothermal influence. The trace and rare earth element concentrations suggest a saline, anoxic and volcanic–hydrothermally-influenced subaqueous environment. In this subaqueous environment of Lucaogou lake, locally high temperatures and a supply of abundant Mg^{2+} from a deep source induced by volcanic–hydrothermal activity formed favourable chemical conditions for direct precipitation of primary dolomite. This study's findings deepen the understanding of the origin and processes of lacustrine primary dolomite formation and provide an alternative possibility for environmental interpretations of ancient dolostones.

Keywords Non-evaporative environment, Permian, primary dolomite, volcanic lake, volcanic–hydrothermal activities.

INTRODUCTION

The occurrence of abundant massive dolostone in the geological record is in sharp contrast to the rarity of modern dolomite, suggesting that most dolomites were altered from other carbonate minerals (Land, 1998; Holland & Zimmermann, 2000; Mazzullo, 2000; Warren, 2000;

Warthmann *et al.*, 2000; Hood *et al.*, 2011). Recently, microcrystalline and disordered dolomite, which is a precursor of ancient well-ordered massive dolomite, has been found in modern and Neogene environments (sabkha flats, hypersaline lagoons, playa lakes, organic-rich deep marine environments and hydrothermal vents) that are saline or hypersaline and have abundant organic materials and/or a large hydrothermal influx (Last, 1990; Arvidson & MacKenzie, 1999; Sanz-Montero *et al.*, 2008; Eickmann *et al.*, 2009; Petrash *et al.*, 2017). The first three environments (sabkha flats, hypersaline lagoons and playa lakes) are commonly evaporative, whereas the last two (organic-rich deep marine environments and hydrothermal vents) are rarely reported due to difficulty in direct field observation.

Compared with the well-studied marine dolomite, lacustrine dolomite is still poorly understood. Last (1990) reviewed over 50 reported world-wide occurrences of modern and Holocene non-detrital dolomites and found that most of the occurrences occur in salt, shallow and/or alkaline lakes which experience intensive evaporation. Dolomite crystals are nano-sized to micro-sized, imperfectly ordered or well-ordered, volumetrically minor, and associated with aragonite, calcite and microbial catalysis in modern and Holocene lakes (Vasconcelos & McKenzie, 1997; Roberts *et al.*, 2004; Cangemi *et al.*, 2016; Petrash *et al.*, 2017), but are volumetrically abundant and associated with evaporitic minerals in ancient deposits (Garcia-Fresca *et al.*, 2018; Cao *et al.*, 2020). Hence, it is speculated that evaporation and later dolomitization are required for the formation of ancient massive dolostones. In those lakes, some of them record strong volcanic–hydrothermal activity; they are termed alkaline lakes and have been reported frequently in recent years (Cangemi *et al.*, 2016; Newell *et al.*, 2017; Yu *et al.*, 2018; Cao *et al.*, 2020; Guo *et al.*, 2021). Those lakes have an extremely high primary productivity, unique environmental conditions and associated carbonate deposits (Southgate *et al.*, 1989; Rothschild & Mancinelli, 2001; Cangemi *et al.*, 2016; Hammond *et al.*, 2019; Cao *et al.*, 2020). Alkalinity, high salinity and concentrations of Na^+, K^+, Mg^{2+} and Ca^{2+} are caused solely by evaporation and, in some cases, with influx of additional materials provided by magmatic water–rock reactions and volcanic–hydrothermal activities (Stamatakis, 1989; Stüeken *et al.*, 2015; Cangemi *et al.*, 2016; Lowenstein *et al.*, 2017; Yu *et al.*, 2018; Hammond *et al.*, 2019; Cao *et al.*, 2020). Hence, chemical elements from a deep source seem to provide additional ingredients for dolomite precipitation but evaporation still seems necessary.

Hydrothermal dolomite, commonly related to fault-controlled dolomitization, formed through alteration by hydrothermal fluid (Davies & Smith Jr., 2006; Smith Jr., 2006; Hollis *et al.*, 2017; Koeshidayatullah *et al.*, 2020). Ilich (1974) first interpreted a genetic type of primary hydrothermal–sedimentary dolomite in the Miocene freshwater deposits of the Inner Dinarides of Yugoslavia. This type has not been the focus of study because the reported modern carbonates in hydrothermal fields consist mainly of aragonite and calcite without a great amount of precipitated dolomite (Kelley *et al.*, 2001, 2005). Nonetheless, studies in the last three decades have shown some dolomite precipitation under various hydrological, geochemical and/or geomicrobiological conditions (Gregg *et al.*, 2015; Hips *et al.*, 2015; Petrash *et al.*, 2017). Dolomite precipitated from a mixture of seawater and hydrothermal fluids is reported from the Logatchev Hydrothermal Vent Field which contains dominantly ultramafic rocks (Eickmann *et al.*, 2009). Furthermore, volcanic and hydrothermal activities in both modern and ancient records commonly show a strong relationship with microbial blooms (Fouquet, 1999; Xie *et al.*, 2010; Procesi *et al.*, 2019), and provide the elements (for example, CO_2, Mg^{2+} and Ca^{2+}), and modify the temperature and pH values that facilitate dolomite precipitation. Recently, some organic-rich lacustrine dolomitic shales have been interpreted as products of volcanic eruption and hydrothermal exhalation, including: (i) the middle Permian Lucaogou Formation in the Santanghu and Junggar basins of north-west China (Liu *et al.*, 2012; Jiao *et al.*, 2018a,b, 2020; Pan *et al.*, 2020; Li *et al.*, 2021; Zhang *et al.*, 2021); (ii) the Cretaceous Tengger Formation in the Erlian Basin of northern China (Yang *et al.*, 2020, 2021); and (iii) the Cretaceous Xiagou Formation in the Jiuquan Basin of south-west China (Zheng *et al.*, 2006; Wen *et al.*, 2013). These studies describe complex depositional and diagenetic environments affected by volcanic–hydrothermal, authigenic and biological processes, which may have promoted the formation of primary dolomitic formation related to hydrothermal activities (Zheng *et al.*, 2006; Liu *et al.*, 2012; Yang *et al.*, 2020).

Nevertheless, it is still unclear whether hydrothermal dolomite precipitation could be a possible mechanism for formation of ancient massive dolostone due to the lack of modern observations. Most ancient dolomites have undergone multiple episodes of diagenesis, which have caused overgrowth and/or recrystallization that mask the primary phase and prevent accurate interpretation of syndepositional environments and conditions (Petrash *et al.*, 2017). Hence, ancient microcrystalline dolomites, especially the lacustrine ones, have been commonly regarded as products of evaporitic environments, even though some lacustrine dolostones do not contain evaporitic features. Thus, the possible primary origin of microcrystalline dolomite without diagenetic alteration and evaporitic features needs to be further studied.

This study reports a suite of laminated dolostones composed mainly of microcrystalline dolomite and minor pyroclastics of the Permian Lucaogou Formation which were deposited in a mixed volcanic–hydrothermal lacustrine environment. This paper provides an alternative interpretation on the origin and processes of lacustrine microcrystalline dolomite formed in a non-evaporitic environment with intense volcanic–hydrothermal activities.

GEOLOGICAL BACKGROUND

The Santanghu Basin is located in the north-eastern Xinjiang Province in north-west China (Fig. 1A). Lacustrine sediments were deposited in a rift basin during the late Carboniferous to middle Permian (Gu *et al.*, 2001; Zhou *et al.*, 2006; Xia *et al.*, 2008; Nan *et al.*, 2016). The basin contains a series of grabens (Fig. 1B; Song *et al.*, 2013), where fluvial–lacustrine sedimentation started in early Permian (Yang *et al.*, 2010). Currently, the basin has five depressions, among which the Malang Depression is the focus of this study.

The middle Permian Lucaogou Formation is the target unit in this study and is sandwiched by two major regional intracontinental volcanic-dominated formations (Fig. S1). The underlying rocks include the upper Carboniferous Haerjiawu Formation and lower Permian Kalagang Formation, which contain a 2500 to 4000 m thick package of intermediate–felsic volcanic rocks. The overlying middle Permian Tiaohu Formation contains *ca* 2000 m thick basalt and tuffaceous shale (Wang *et al.*, 2015). The Lucaogou Formation is a regional hydrocarbon source rock and is dominantly comprised of well-laminated dolomite-rich fine-grained sedimentary rocks, including dolostone, shale, tuff and minor sandstone, which were deposited in a sediment-starved profundal lake with a stratified, saline environment (Fig. 1; Feng *et al.*, 2004; Liu *et al.*, 2012; Hackley *et al.*, 2016; Liu *et al.*, 2020). It averages 200 m in thickness but locally can be up to 600 m thick. Recent studies have reported volcanic–hydrothermal sediments in the formation (Jiao *et al.*, 2018a,b, 2020; Liu *et al.*, 2020; Pan *et al.*, 2020; Zhang *et al.*, 2021). For example, tuffaceous grains are common in most lithofacies. Some intervals contain concentrated basic, intermediate and/or felsic pyroclastic sediments. Many cone-shaped bodies on seismic sections within the Lucaogou Formation (Fig. S2) are composed dominantly of volcanic–hydrothermal deposits (Fig. 1B and C; Jiao *et al.*, 2018a). The predominant lithofacies is a shale, composed mainly of angular alkaline feldspars, some quartz and dolomite, and minor or no clay minerals (smectite) and are identified as tuffaceous shale. They are interpreted to be of a volcanic origin with hydrothermal alteration (Jiao *et al.*, 2020; Pan *et al.*, 2020; Zhang *et al.*, 2021). In summary, regional volcanism was intensive before and after the deposition of the Lucaogou Formation, but relatively weak during its deposition as a continuation of Haerjiawu and Kalagang volcanism and/or precursor to the Tiaohu volcanism.

DATA AND METHODS

Texture and composition of dolostones in the Lucaogou Formation were documented in the context of large-scale stratigraphy and microscopic petrography by using seismic, well log, mud log, core, petrographic and geochemical data. First the total thickness of the formation and distribution of dolostones and igneous rocks was determined by examination of 40 wells in the Malang Depression. The data were compared with the distribution of volcanic and hydrothermal fields interpreted from seismic data by Jiao *et al.* (2020) to define the overall sedimentary setting. Second, approximately 200 core segments from 28 wells with a total thickness of *ca* 800 m were described to document the sedimentary structures of dolostone and their stratal

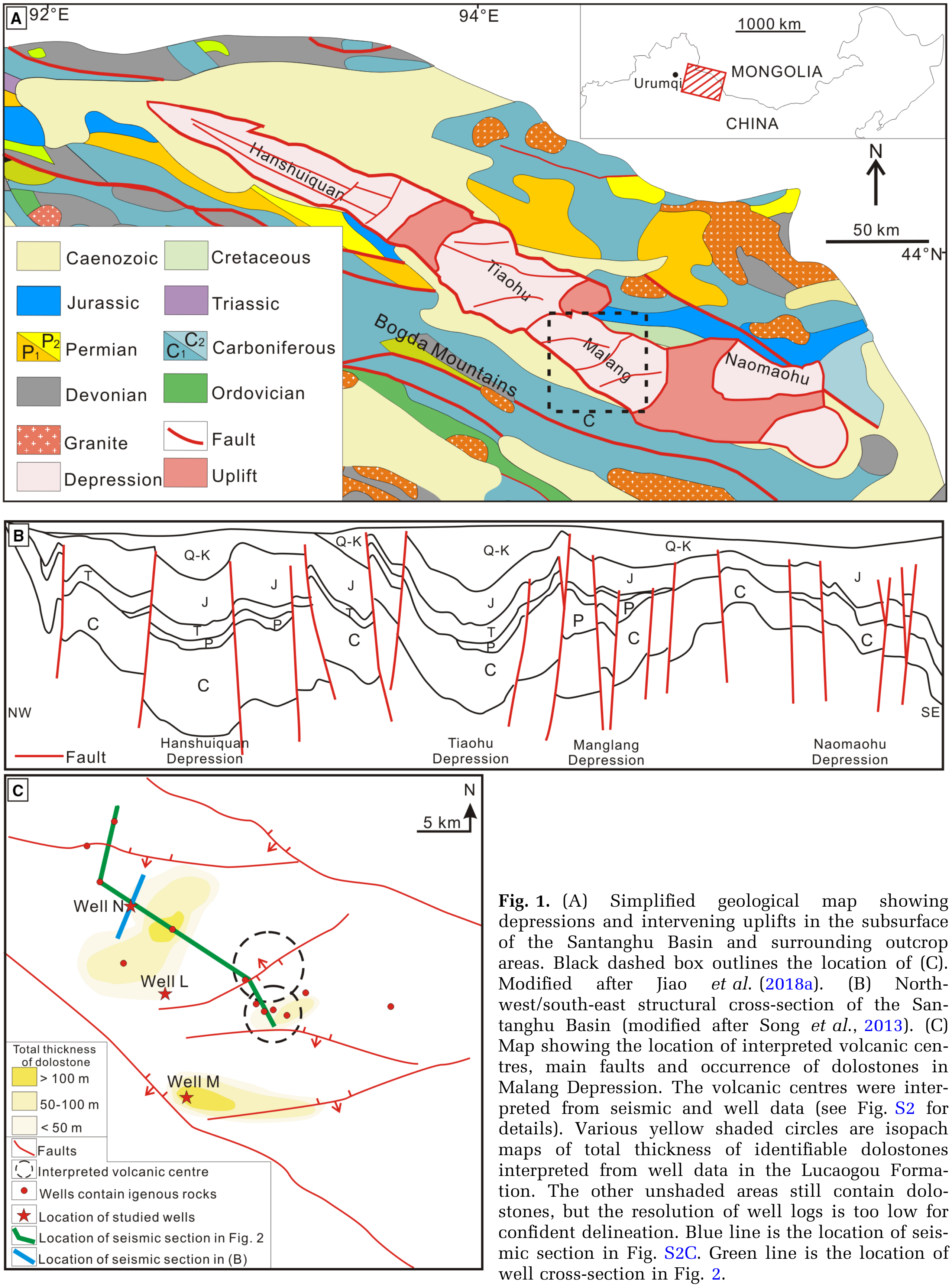

Fig. 1. (A) Simplified geological map showing depressions and intervening uplifts in the subsurface of the Santanghu Basin and surrounding outcrop areas. Black dashed box outlines the location of (C). Modified after Jiao *et al.* (2018a). (B) North-west/south-east structural cross-section of the Santanghu Basin (modified after Song *et al.*, 2013). (C) Map showing the location of interpreted volcanic centres, main faults and occurrence of dolostones in Malang Depression. The volcanic centres were interpreted from seismic and well data (see Fig. S2 for details). Various yellow shaded circles are isopach maps of total thickness of identifiable dolostones interpreted from well data in the Lucaogou Formation. The other unshaded areas still contain dolostones, but the resolution of well logs is too low for confident delineation. Blue line is the location of seismic section in Fig. S2C. Green line is the location of well cross-section in Fig. 2.

relationship with adjacent strata and to conduct representative sampling. Finally, 38 dolostone core samples from three wells were selected for thin-section petrographic observations.

Samples were preliminarily classified on the basis of mineral composition, texture, structure and content of volcanic clasts. Thirty-eight samples of dolostone laminae identified under polarized microscope (BX51; Olympus Corporation, Tokyo, Japan) were collected by microdrilling to document their mineral composition and crystallinity using an X-ray diffractometer (D/MAX-2500; Rigaku Corporation, Tokyo, Japan). Then, 18 samples with more than 50% dolomite were selected for geochemical analysis.

The microscopic structures and textures of the 18 samples were documented in detail to establish a solid context for interpretation of geochemical data. Firstly, the samples were cut perpendicular to bedding plane into two pieces, one for microscopic observation (well-polished under a stereoscopic microscope; Figs S3 and S4), the other for geochemical, microprobe and scanning electron microscopic (SEM) analyses. Second, the high-resolution crystal textures of dolomite and coexisting quartz and feldspar were observed under SEM [FEI Helios NanoLab 600 (SEM/FIB); ThermoFisher Scientific, Waltham, MA, USA]. Third, the major chemical compositions and crystal size and shape of dolomite crystals were obtained using a JXA-8100 electron microprobe (JEOL Limited, Tokyo, Japan) with a beam spot size of 1 μm. A total of 90 test points (30 test points for each sample from the three wells) were analysed. Fourth, the homogenization temperatures of six representative fluid inclusions in dolomite crystals (Fig. S5) were obtained using a cooling–heating stage [THMS600 (testing range from −196 to 600°C, error ±1°C); Linkam Scientific Instruments Limited, Salford, UK]. Finally, the target laminae of dolostones were sampled by microdrilling (see the sampled laminae of each studied dolostones in Fig. S3). The powder was analysed for isotopic compositions of C, O, Sr, Mg, trace elements and rare earth elements (REEs). The Sr, Mg, trace elements and REEs were analysed using a Nu Plasma Multi-Collector Inductively Coupled Plasma Mass Spectrometer (MC-ICP-MS; Nu Instruments Limited, Wrexham, UK), while the C and O isotope compositions were determined using a MAT252 mass spectrometer (ThermoFisher Scientific, Waltham, MA, USA). All analyses were reported in delta notation as per mil (‰) and were conducted at the State Key Laboratory of Continental Dynamics at Northwest University, Xi'an, Shaanxi, China.

RESULTS AND INTERPRETATION

Co-occurrence of dolostone and volcanic deposits

Igneous rocks are mainly basalt with rare andesite and were identified in 14 out of 40 studied wells from wireline and mud logs (Fig. 1C). The wells that intersect igneous rocks are mainly located in the central part along the main fault of the Malang Depression, which also has volcanic centres identified from seismic and core data (Figs 1C and S2; see details in Jiao *et al*., 2018a). The igneous rocks are commonly intercalated within tuffaceous shale and range from 0.5 to 5.0 m (mostly 1 m) in thickness. The occurrence of dolostones is non-uniform but concentrated in three areas close to three main faults and around the volcanic centres (Fig. 1C). For example, lithofacies in Well 7 are mainly tuffaceous shale with several intervals of tuff (Fig. 2). A total of three layers of basalt and no dolostones were observed. In contrast, lithofacies in wells 101 and ×1 (Fig. 2) are interbedded tuffaceous shale and dolostone with minor tuff. Wells containing abundant dolostones are about 5 km away from the volcanic centres and also distributed along the three main faults in the depression (Fig. 1C).

Petrological characteristics of dolostones

Several microscopic characteristics of dolostone provide strong evidence supporting the close association of dolomite formation with volcanic processes. Firstly, dolostones are intercalated or interbedded with tuffaceous shales of a volcanic origin with hydrothermal alterations (Fig. S4; Jiao *et al*., 2020). The dolostones contain a variety of non-dolomite grains of a variable amount ranging from 14 to 48%. The grains are mainly monomineralic silicate minerals, vitric fragments, smectite, quartz, magnesite (Fig. S6) and serpentine of a trace amount. Furthermore, less than 2% of calcite is detected in some dolostones. The calcite occurs as vein filling and does not appear to be related to dolomite formation. The dolostones are classified into three types on the basis of the type, amount and origin of the non-dolomitic grains as pyroclastic-poor (Type I), vitric and crystal-rich (Type II) and smectite-rich (Type III), reflecting a

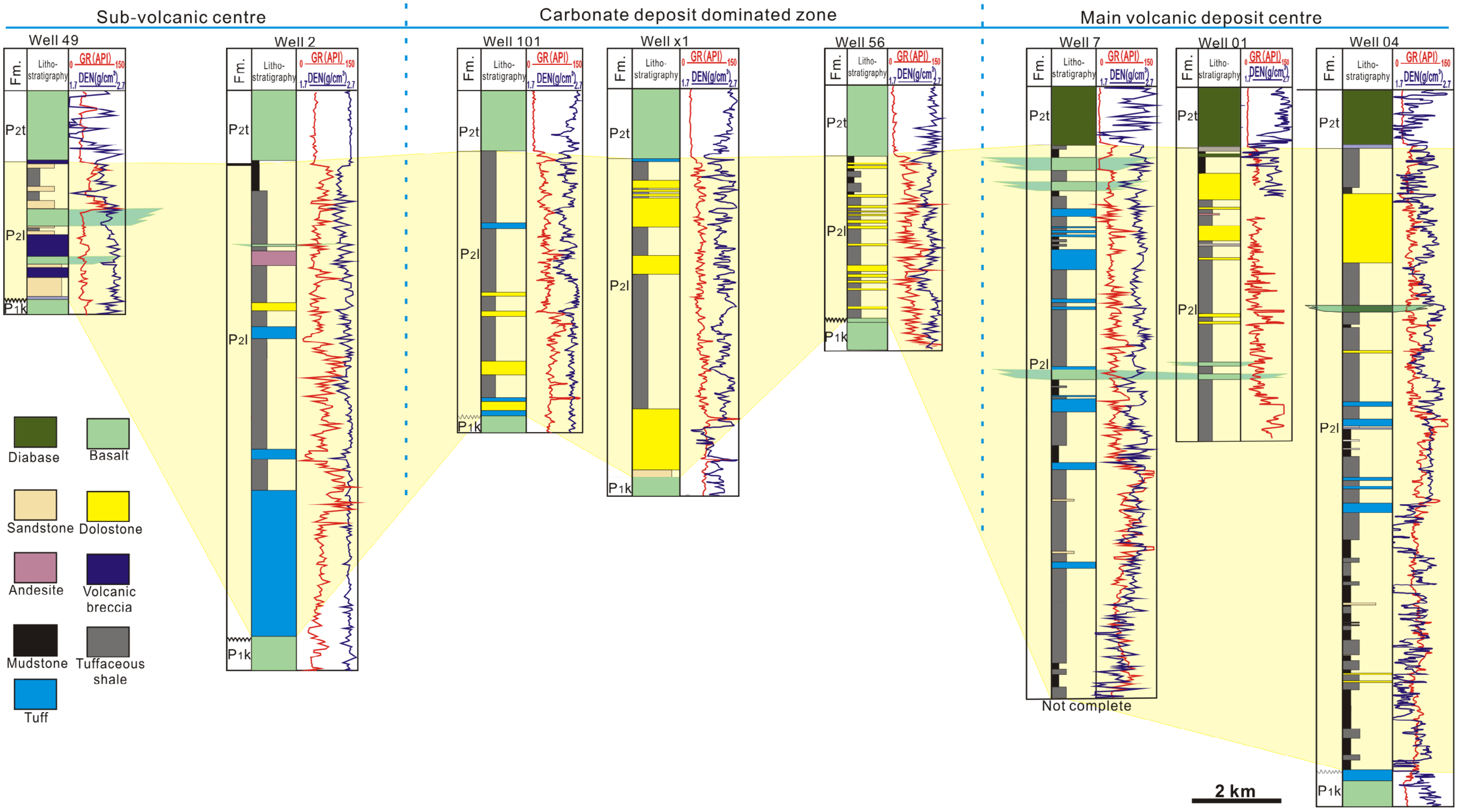

Fig. 2. Stratigraphic well cross-section showing the correlation of the Lucaogou Formation from north-west to south-east in the Malang Depression, demonstrating lateral and vertical lithofacies changes. The main volcanic centre occurs mainly in the central Malang Depression close to Well 7 and is composed mainly of tuff and minor basalt. The lithofacies were interpreted from well logs, mud log data and cores. See Fig. 1C for section location. GR – gamma ray. Den – density.

varying degree of influence of volcanic and hydrothermal processes during the formation of dolomite. Their characteristics and interpretations are described in detail below.

Type I pyroclastic-poor dolostone

Description. This type of dolostone is the most abundant among the three types. It is well-laminated and individual laminae range from 50 μm to 1 mm thick. The dolostone laminae are brown, dominantly planar and parallel and, in rare cases, brecciated and exhibit soft-sediment deformation. They alternate with black to dark-brown organic-rich laminae to form a lamina set with a thickness ranging from 1 to 50 cm (Fig. 3A to C). The organic-rich laminae are 5 to 30 μm thick and have uneven thickness and wavy bedding surfaces (Fig. 3D). The lamina sets are interbedded with tuffaceous shale with a sharp and planar contact (Fig. 3C). This type of dolostone is composed mainly of dolomite (63.2 to 85.0%, average = 80.4%; Table 1) and quartz (5.7 to 32.0%, average = 13.6%) and a small amount of K-feldspar, calcite, smectite, analcite and pyrite.

Dolomite crystals are mostly smaller than 2 μm in size and have a euhedral to subhedral shape with smooth crystal edges (Fig. 3E to G); some dolomite crystals close to the organic-rich laminae range from 2 to 10 μm in size and are associated with pyrite (Fig. 3F). The cation ordering of dolomite ranges from 0.36 to 0.46 (average of 0.42). A trace amount of dolomite crystals are 10 to 30 μm in size, euhedral rhombic and filling a local fluid escape structure and adjacent microcrystalline dolomite-dominated laminae (Fig. S6A and B). Their crystals are partially replaced by magnesite in association with pyrite precipitation.

Non-dolomite grains include angular shard-like and rounded quartz and feldspar. They are scattered discretely and randomly in the dolomite matrix (Fig. 3E). As the most abundant non-dolomite mineral (Table 1), quartz occurs in variable amounts in the samples and show four types of textures in this type of dolostone. The first type has a shard shape (Fig. S6C). The second type has a hexagonal columnar shape with a pinnacle on one end and a smooth fracture surface on the other end (Fig. S6D). In addition, the surfaces of the above two types of quartz crystals are smooth without scratches (Fig. S6C and D). The third type is rounded and silt in size (Fig. 3E). The fourth type of quartz is rare. It fills in vertical micro-fractures with a euhedral form (Fig. S6E). The feldspar grains are orthoclase and also shard-like.

Interpretation. The main types of quartz are of pyroclastic or terrigenous origin. The first type suggests an origin of devitrified volcanic glass (Fig. S6C). The morphological features and smooth surfaces (Fig. S6D) of the second type indicate that the quartz crystals were precipitated from water or crystalized from magma and then fractured and had been transported for a short distance as bedload or suspension load without frequent abrasions (Jiao *et al.*, 2020). The third type (Fig. 3E) is of terrigenous and detrital origin. The fourth type (Fig. S6E) is interpreted as autogenetic precipitate formed during the late diagenetic stage and causing the high quartz content in some samples (for example, Sample N-5 in Table 1). Furthermore, the relationship between partially replaced dolomite and magnesite (Fig. S6A and B) indicates that a Mg-rich fluid was present in local interstitial water during deposition and may have caused dolomite recrystallization. Relatively large dolomite crystals close to the organic-rich laminae (Fig. 3F) may also be affected by dolomite recrystallization. In the meanwhile, the co-

Fig. 3. Photographs showing the structures, composition and texture of Type I pyroclastic-poor dolostone. (A) Vertical cut of a polished core showing parallel laminations. The dark grey laminae are rich in organic matter. (B) Upward changes from brecciation, soft-sediment deformation, to lamination. Dark grey matrix in the brecciated and soft-sediment deformed parts are mainly dolomite with abundant organic matter. (C) Laminated dolostones are sandwiched by black tuffaceous shale (red arrows) with sharp and planar contacts. (D) A close-up of (A) showing that dolostones are interlaminated with irregular and discontinuous dark brown organic-rich laminae. Plane polarized light (PL). (E) A close-up of (D) showing dolostone lamina containing discrete shard-like pyroclastic (red arrows), rounded terrigenous clastic (yellow arrow) and brown to dark brown organic matter grains. PL. (F) Backscatter electron microprobe image of (A) showing generally subhedral to euhedral dolomite crystals. The black organic-rich lamina is concave–convex and bent or wrapped around the dolomite crystals. Bright white grains are pyrite. (G) Scanning electron photomicrograph of (A) showing dolomite crystals that are *ca* 3 μm in size and euhedral with straight and smooth edges, very fine dolomite (smaller than 1 μm; red arrows) and smectite fill in the intercrystalline pores. The vertical white and dark grey veins in (A) to (C) are artificial.

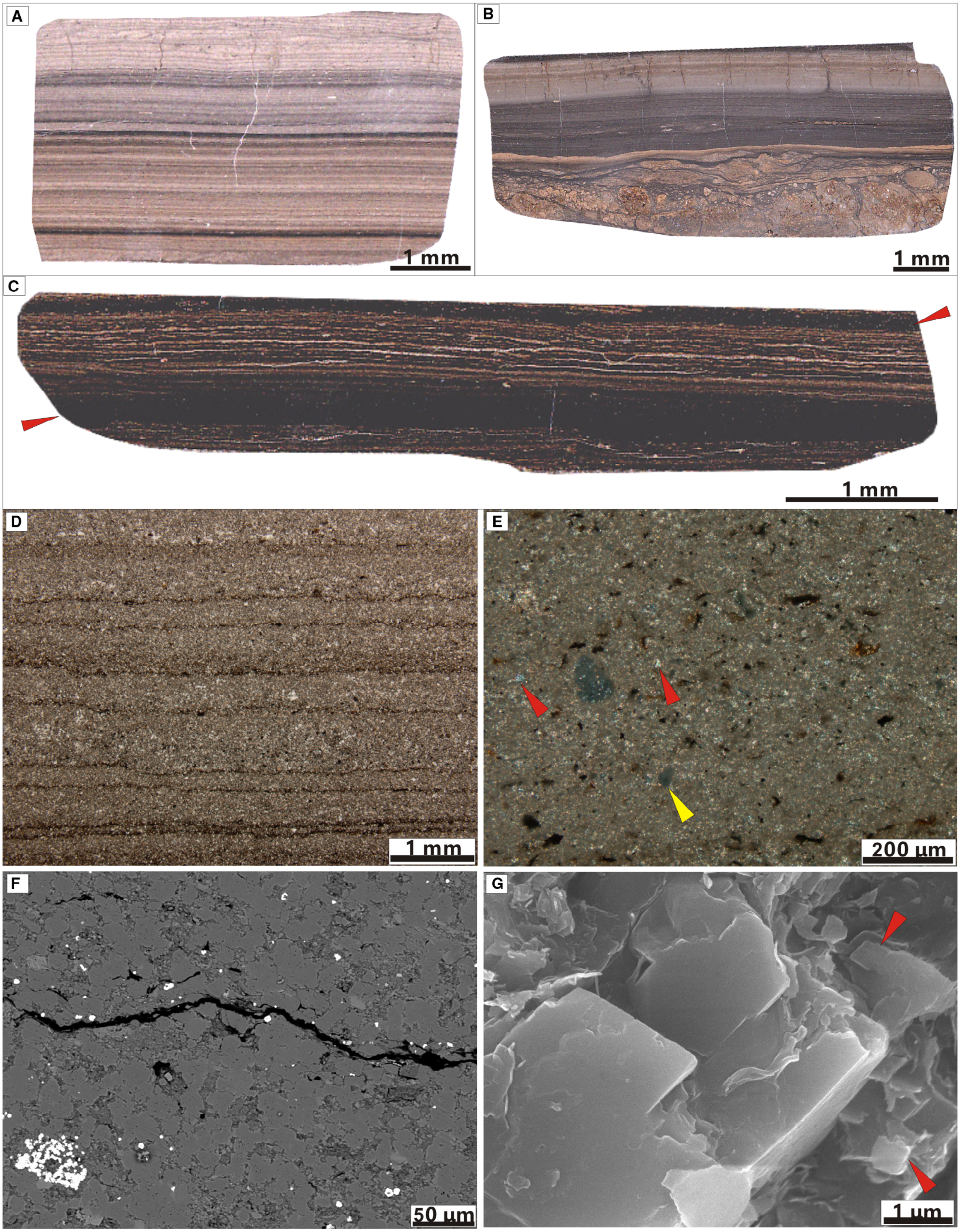
A
1 mm
B
1 mm
C
1 mm
D
1 mm
E
200 μm
F
50 μm
G
1 μm

occurrence of pyrite and large dolomite crystals only occurs close to the organic-rich laminae and in micro-fractures. This indicates that some alteration, including pyrite precipitation and dolomite recrystallization, occurred after the nucleation of small dolomites. Hence, the dolomites in Type I dolostone are interpreted as predominantly precipitates on the lake floor with later and local recrystallization. A small amount of terrigenous and pyroclastic sediments were mixed with the dolomite through suspension settling.

Type II vitric and crystal-rich dolostone

Description. Type II dolostone is common in all samples. It is well-laminated with individual laminae ranging from 80 μm to 1 cm thick. Most dolomite laminae are interlaminated with organic-rich laminae to form lamina sets similar to those in Type I dolostones (Fig. 4A). However, many lamina sets are convoluted and intercalated within planar and parallel lamina sets, showing syndepositional soft-sediment deformation, not later tectonic deformation. Some lamina sets are cross-laminated (Fig. 4A). Only one thick (0.5 to 1.0 cm in thickness) lamina is internally massive and intercalated with tuffaceous shale with sharp contacts (Fig. 4B). The mineral composition of Type II dolostone (Table 1) includes dolomite (66.8 to 86.0%, average = 77.3%), quartz (8.9 to 22.0%, average = 13.5%), plagioclase (2.8 to 6.5%, average = 4.5%), analcite (0.6 to 6.3%, average = 3.1%) and rare calcite. In comparison to Type I dolostone, Type II dolostone contains plagioclase, not K-feldspar, and about 2% more analcite.

Dolomite crystals in this type are similar to those in Type I dolostone, mostly smaller than 2 μm with some 3 to 8 μm in size (dolomite close to organic-rich laminae). Their cation ordering ranges from 0.35 to 0.44, and 0.40 on average. However, crystals are highly euhedral (Fig. 4C and D) with smooth crystal edges. Non-dolomite grains are dominantly volcanic-originated vitric and crystal grains due to their typical shard-like shape and non-extinction under cross-polarized light (Fig. 4E to H). The grains mainly occur close to the adjacent organic-rich laminae (Fig. 4E and F) and are discretely scattered in thick dolostone laminae (Fig. 4G and H). The monomineralic grains are quartz and feldspars with an angular shape and rare embayed edges (Fig. 4F). Rounded quartz grains were not observed. Analcite grains with an angular and shard-like shape are scattered in microcrystalline dolomite-dominated matrix (Fig. S6F). A few clay-sized analcite grains serve as matrix filling intercrystalline pores of dolomite crystals (Fig. S6G).

Interpretation. Generally, analcite has three origins. Most commonly, it is a diagenetic mineral transformed from volcaniclastics at a very early stage (Wilkinson, 1977) and from detrital smectite in alkaline water (Hay *et al.*, 1991). It can also form in saline solution through replacement of K^+ by Na^+ of leucite in leucophonolite or nepheline in phonolite, both of which are common in peralkaline extrusive rocks (Gupta & Fyfe, 1975; Roux & Hamilton, 1976; Wilkinson, 1977). Last, analcite can crystallize directly from peralkaline magma to form analcite phonolite (Jiang *et al.*, 2008) or from peralkaline hydrothermal fluid to form mineral assemblages of dolomite–analcite–pyrite in mudstone (Li *et al.*, 2021). The shard-like shape of analcite framework grains suggests that they may have been formed by replacement of the original volcanic vitric grains (Fig. S6F). The pore-filling analcite is too small to define the grain geometry but is probably of the same replacement origin (Fig. S6G). Furthermore, the euhedral crystals with smooth edges of dolomite, as well as the strong angularity of the non-dolomite grains indicate that they had experienced minimal or no abrasion and, thus, current transport.

Above all, Type II dolostones show a strong syndepositional relationship with volcanic fragments. The dolomites are interpreted as *in situ* chemical precipitate on the lake floor and mixed with vitric and crystal grains settled from suspension in the water column. The lake water is of relatively low energy with episodic local turbulence. Local disturbance induced by, for example, volcanic eruptions, and facilitated by a steep topography may have caused syndepositional soft-sediment deformation. The massive pyroclastic grains in the thick lamina (Fig. 4B, G and H) are interpreted as a density-flow deposit.

Type III smectite-rich dolostone

Description. Type III dolostone is characterized by a 'porphyritic' texture and abundant smectite content. It is only common in Well L, which is close to the volcanic-dominated field. A total of 15 beds are present. The beds are 3 to 12 cm thick and intercalated with tuffaceous shale with conformable and sharp contacts. This dolostone

Table 1. Petrological features of laminated dolostones (types I pyroclastic-poor and II vitric and crystal-rich dolostones) from the Lucaogou Formation, Santanghu Basin.

	Mineral composition (wt. %)*								Sedimentary structure		Dolomite texture			
Sample No.	D	P	K	Q	A	C	S	Pr	Thickness (mm)†	Geometry	Size (μm)‡	Shape	Order degree	Other features
M-1	75.5	5.4	0	13.0	6.3	0	0	0	2.0–3.0	Parallel	1–22, 3–8	Euhedral–subhedral	0.42	Oil-bearing; rich in shard-like quartz and analcite. Sandwiched by tuff with sharp boundaries; algal mat
M-2	66.8	2.8	0	22.0	3.6	5.0	0	0	0.08–0.2	Parallel	1–18, 2–10	Subhedral– euhedral	0.38	Oil-rich; rich in angular and bedding-parallel quartz; algal mat
M-3	80.7	6.5	0	8.9	2.0	2.0	0	0	0.1–0.3	Parallel, soft-deformation	2–19, 3–10	Euhedral– subhedral	0.35	Oil-rich; angular quartz grains are bedding-parallel and show normal grading; algal mat; biotic build-ups
M-8	86.0	3.1	0	10.0	0.6	0	0	0	0.8–2.0	Parallel	1–14, 2–10	Subhedral– euhedral	0.44	Oil-bearing; rich in angular and bedding-parallel quartz
N-2	82.7	0	0.4	13.0	2.7	0	2.0	0	0.05–1.0	Parallel, brecciated	1–15, 2–6	Subhedral– euhedral	0.41	Oil-bearing; some brecciated dolostones accumulate in one dolomitic lamina
N-3	84.2	0	0.9	7.3	0	4.0	4.0	0	0.1–0.8	Parallel	2–20, 2–15	Subhedral– euhedral	0.46	Oil-bearing; angular quartz grains bearing; algal mat
N-5	63.2	0	0.9	32.0	0	1.0	1.0	2.0	0.05–1.0	Parallel	1–13, 2–6	Anhedral– subhedral	0.36	Oil-bearing; angular quartz grains bearing; algal mat; biotic build-ups
N-11	82.4	0	1.3	14.0	0	1.0	1.0	0	0.1–0.3	Parallel	1–10, 2–6	Anhedral– subhedral	0.42	Oil-bearing; biotic build-ups
N-15	84.7	0	0.3	9.4	0	6.0	0	0	0.05–1.0	Parallel	1–11, 2–8	Anhedral– subhedral	0.44	Oil-rich; angular quartz grains bearing; algal mat; biotic build-ups
N-24	85.0	0	9.3	5.7	0	0	0	0	0.05–0.1	Parallel	2–18, 3–12	Subhedral– euhedral	0.45	Oil-rich; interlaminated with tuffaceous shale; algal mat

* The mineral composition of dolostone and the order degree of dolomite are determined by X-ray diffraction (XRD). D – dolomite, P – plagioclase, K – K-feldspar, Q – quartz, A – analcime, C – calcite, S – smectite, Pr – pyrite. † Thickness = thickness of individual lamina. ‡ Size of individual dolomite crystal size measured under backscatter images using a microprobe. The left part of crystal size data is the overall range, whereas the right part is the most frequent range. The grain size of quartz, feldspar and analcite in dolostones is mainly silt sized.

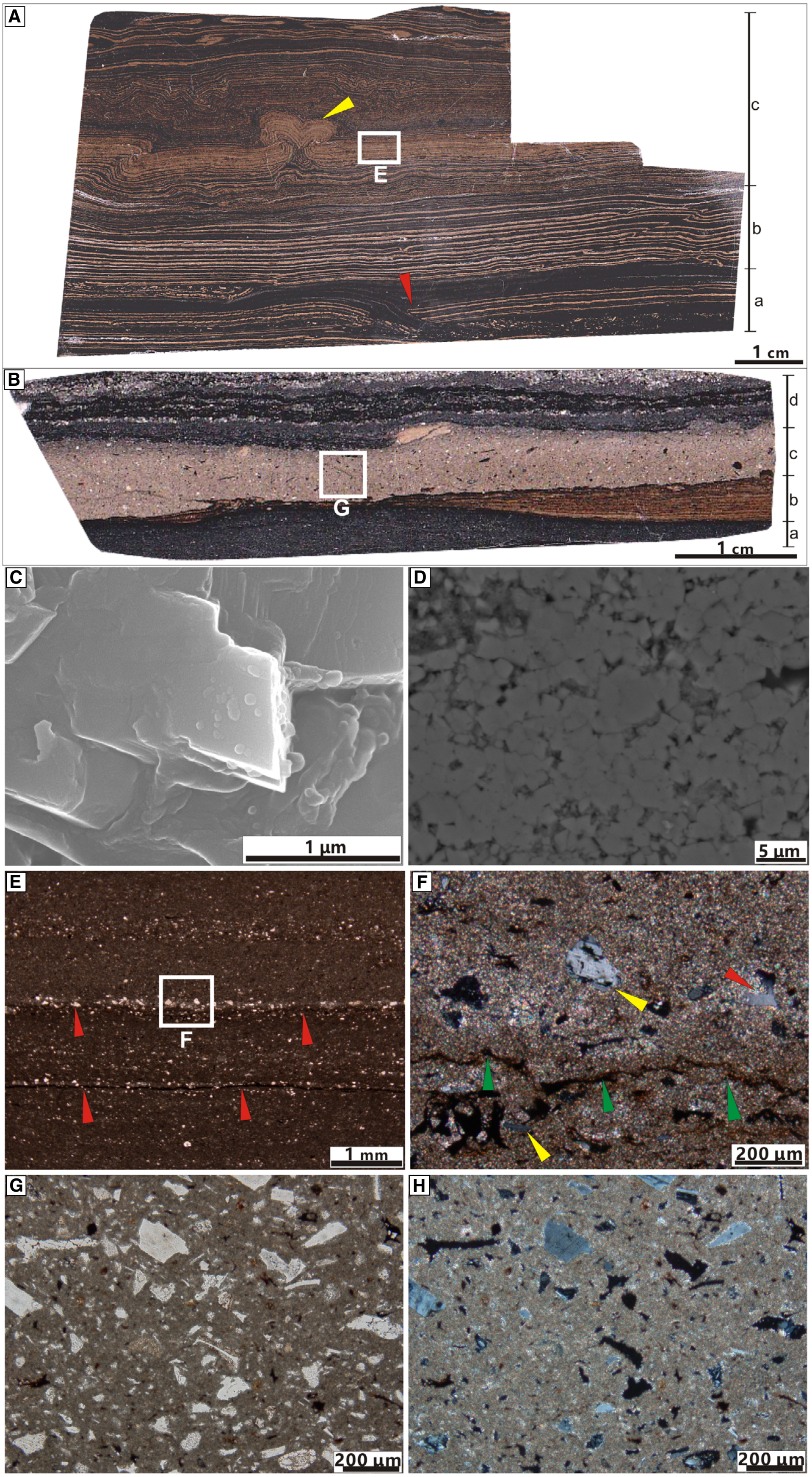
A
E
c
b
a
1 cm
B
G
d
c
b
a
1 cm
C
1 µm
D
5 µm
E
F
1 mm
F
200 µm
G
200 µm
H
200 µm

Fig. 4. Photographs showing structures, composition, and texture of Type II vitric and crystal-rich dolostone. (A) Vertical cut of a polished core showing micro-scale sedimentary structures, especially laminations. The black laminae are rich in organic matter. The sample contains three lamina sets that are cross-laminated (Set a; red arrow), parallel laminated (Set b) and soft-sediment deformed (Set c; yellow arrow). (B) Two dolostone lamina sets (b and c) are intercalated with two laminae of tuffaceous shale (a and d) with sharp boundaries. Set b is laminated, while Set c is massive. (C) A scanning electron microscope (SEM) image showing the euhedral dolomite crystals *ca* 1 μm in size. (D) Backscatter electron microprobe image showing the dolomite crystals are generally subhedral to euhedral, and 1 to 3 μm in size. (E) A close-up of box E in (A). Dolostones are interlaminated with continuous to discontinuous wavy organic-rich laminae (red arrows). Pyroclastic grains (white) occur close to the organic rich laminae. Plane polarized light (PL). (F) A close-up of box F in (E) showing that pyroclastic grains (yellow arrows) are typically shard-like, vitric, angular, monomineralic and occur close to the organic-rich lamina (green arrows). Some grains show embayed edges (red arrow). Cross-polarized light (XL). (G) A close-up of box G in (B) showing the internal massive structure of a thick lamina of dolostone. Bright grey pyroclastic grains occur in bright brown microcrystalline dolomite matrix discretely. PL. (H) The same as (G) showing grain extinction patterns of vitric (black) and felsic (grey) pyroclastic grains.

is mainly massive and contains rare crudely vertical fluid escape structures and associated deformed wavy laminae (Fig. 5A and B). Dolomite and smectite dominate (Table 2), ranging from 51.9 to 73.3% (average = 59.5%) and 20.1 to 43.5% (average = 34.4%), respectively. Other minerals include feldspars (5.3% on average) and rare pyrite. The cation ordering of dolomite ranges from 0.35 to 0.65 (average = 0.50).

Sand-size grains (i.e. the porphyritic grains) float in the dark grey matrix (Fig. 5A and B). They are aggregates of fine (10 to 40 μm) dolomite crystals and smectite with minor feldspars (Fig. 5C and D). The matrix is also composed of the same minerals, but non-aggregated (Fig. 5E). In the aggregates, dolomite crystals dominate and are mainly euhedral to subhedral with smooth crystal edges. Clay-sized smectite fills the intercrystalline pores (Fig. 5D). In the matrix, dolomite crystals are relatively small and anhedral with concave–convex edges, and float in smectite-dominated matrix (Fig. 5E). The concave–convex edges indicate partial dissolution. Feldspars are mainly albite and orthoclase, subhedral to anhedral, and also show partial dissolution (Fig. 5E). Dolomite in deformed wavy laminae and fluid escape structures are highly euhedral; some of the coarse crystals are replaced by serpentine along the edges (Fig. 5F and G). Six fluid inclusions (Fig. S5) in the dolomite crystals have a homogenization temperature ranging from 56.2 to 86.0°C (average = 74.7°C).

Interpretation. Smectite is the dominant mineral in Type III dolostone, but only in a trace amount in Type I and is absent in Type II (Tables 1 and 2). Generally, it may have formed by alteration of basic volcanic rocks by acidic fluids or by alteration of volcanic ash in lake water (Gill, 2010). In addition, the occurrence of fluid escape structures (Fig. 5F and G) suggests that acidic hydrothermal fluid had altered the dolomite (Gill, 2010) before dolomite lithification. Therefore, the smectite is interpreted to have an origin of altered volcanic ash on the basis of its matrix distribution. Furthermore, feldspars occur in all three types of dolostones. They are alkaline feldspars of orthoclase and albite, as determined by Jiao *et al.* (2020), and unevenly distributed among the three types of dolostone (Tables 1 and 2). Albite only occurs in Type II dolostone; orthoclase only in Type I; and both types of feldspars in Type III. The occurrences indicate that the feldspars were derived from locally distinct sources. Finally, feldspar grains in Type III dolostone are dominantly anhedral with concave and convex edges, which are interpreted to be caused by dissolution (Figs 5E and S6H). In contrast, feldspar grains in types I and II dolostones are euhedral or angular with sharp edges (Fig. 4F and G), indicating no or weak dissolution.

Type III dolostones are interpreted as reworked pyroclastic debris-flow deposits when dolomite crystals were precipitated but not solidified. The composition and texture of aggregates (Fig. 5C and D) suggest successive aggregation of original dolomite crystals and matrix through collision at a relatively high temperature and wet environment in the debris flow (e.g. Schumacher & Schmincke, 1995). The smectite is probably altered volcanic ash by local acidic hydrothermal fluid. The fluid escape structures and soft-sediment deformation indicate that the original sediments were water-saturated and not fully consolidated (Garcia-Fresca *et al.*, 2018).

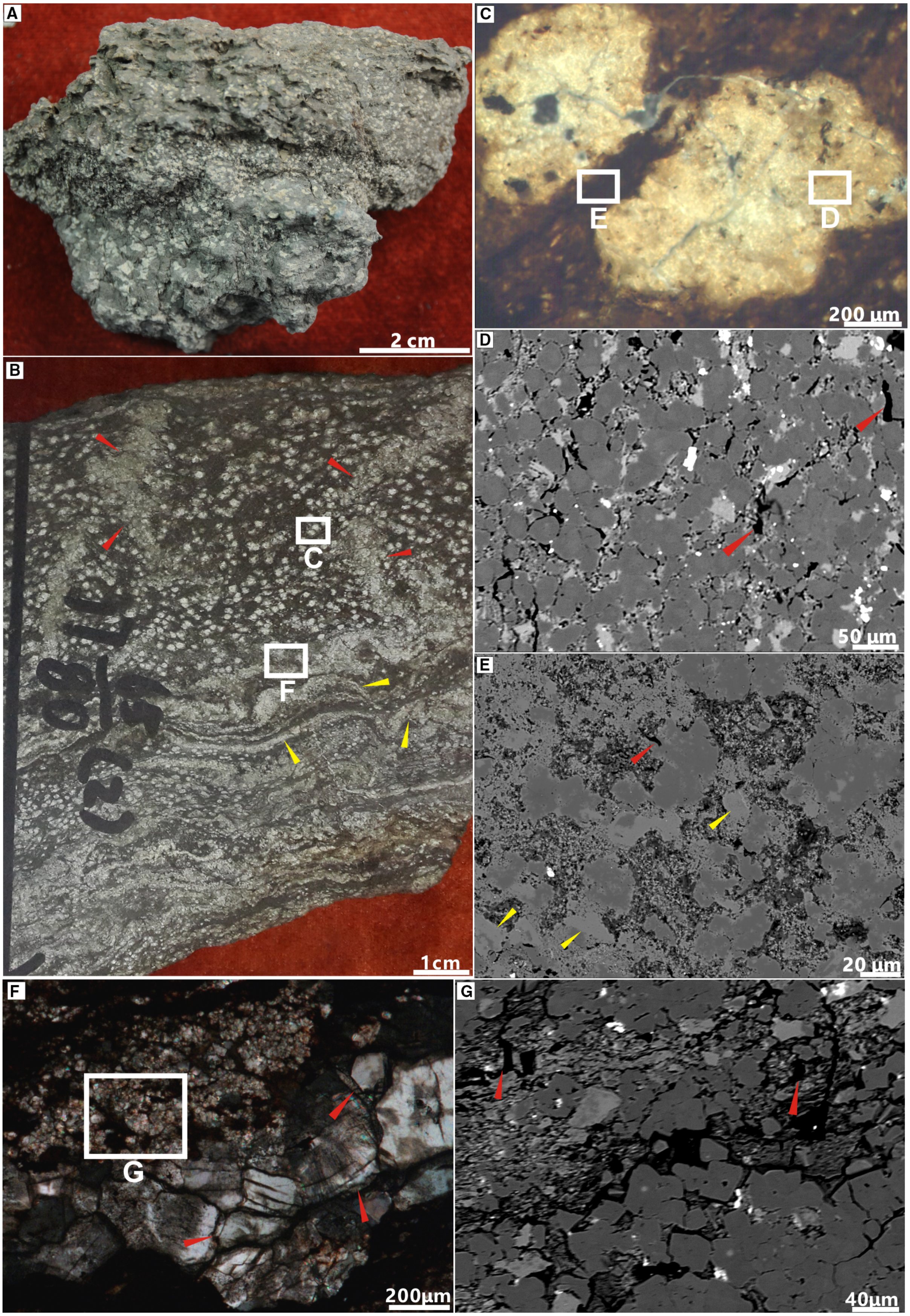
A
2 cm
C
E
D
200 µm
B
C
F
1cm
D
50 µm
E
20 µm
F
G
200µm
G
40µm

Fig. 5. Photographs showing sedimentary structure, composition and texture of Type III smectite-rich dolostone. (A) Core with a massive structure. White phenocrysts are scattered in grey matrix. (B) Vertical cut of a core showing the massive structure, local soft-sediment deformation structures (yellow arrows) and water escape conduits (red arrows). (C) Thin-section photomicrograph of box C in (B) showing two yellow-grey phenocrysts in dark brown matrix. Plane polarized light (PL). Black grains are pyrite. (D) Backscatter electron microprobe image of box D in (C) showing the internal structure and mineral compositions of the phenocrysts. The grains are not monomineralic but an aggregate of dolomite, which is dark grey, subhedral to euhedral, 10 to 40 μm in size, as framework grains, and smectite filling intercrystalline pores with rare light grey alkaline feldspars and organic fragments (red arrows). White grains are pyrite. (E) Backscatter electron microprobe image of box E in (C) showing features of matrix. Similar to the aggregate grains, the matrix is also composed of dark grey dolomite, light grey alkaline feldspars (yellow arrows), and smectite filling intercrystalline pores with variable proportions. Rare irregular organic fragments are present (red arrow). Dolomite and alkaline feldspars are mostly subhedral to anhedral with concave–convex edges and embedded in smectite matrix. (F) Thin-section photomicrograph of box F in (B) showing soft-sediment deformed laminae. Dolomite crystals are well recrystallized and *ca* 200 μm in size with edges replaced by serpentine (red arrows). XL. (G) Backscatter electron microprobe image of box G in (F) showing a water escape conduit. Dark grey dolomite crystals are euhedral with smooth edges. Light grey grains are alkaline feldspars. Smectite fills in intercrystalline pores. Black irregular grains are organic fragments (red arrows). (G) is modified after Jiao *et al*. (2018a).

Microbial deposits in dolostones

Abundant microbial laminations and microbial build-ups (1 to 2 mm in width and 0.1 to 0.5 mm in height) with some microbial crusts and mineral filaments occur in types I and II dolostones (Figs 6 and S7). Only a small amount of irregularly shaped organic fragments are observed in Type III (Fig. 5D, E and G). Microbial laminations are very common in types I and II dolostones and interlaminated with dolostones. The laminae are *ca* 10 μm thick, crenulated and sub-parallel (Fig. 6A to D) and contain abundant alginite (Fig. 6E and F). These features suggest that the laminated deposits are lamalginite. Detrital grains are present close to the organic-rich laminae in the neighbouring laminae (Fig. 4E and F), suggesting that the grains are organically bound. In addition, organic-rich cone-shaped bodies are present in types I and II dolostones (Fig. 6A to D). The bodies are a few millimetres wide with a flat base and a peaked top, and commonly confined in a single lamina. The geometry and high organic content suggest that the bodies are possible microbial build-ups. This interpretation is supported by their close spatial relationship with lamalginite.

Furthermore, many possible microbial crusts (Fig. S7A to D) and irregularly curved filamentary minerals (1 μm long and approximately hundreds of nanometres wide; Fig. S7E and F) are present in types I and II dolostones. They are closely intergrown with dolomite. However, the exact species of the crust cannot be identified. The filamentary minerals are not illite or mordenite which is supported by the absence of clay minerals in XRD results of Type II dolostone (Table 1). The filamentous structure is similar to the biomass of dolomite-rich microbial mats in the modern sabkha (Petrash *et al*., 2017). The intertwining relationship between the microbial crusts, filamentary minerals and dolomite cannot provide direct evidence that the nucleation of studied dolomite is related to microbial activities, but at least suggests coeval microbial activity and dolomite formation and accumulation.

Geochemical characteristics of dolostones

The three types of dolostones exhibit respective unique geochemical characteristics, indicating variable depositional and diagenetic processes in different environments. Most importantly, dolomite crystals in the analysed samples are dominantly microcrystalline without recrystallization. Hence, the samples likely have not been significantly altered during diagenesis and contain information on the original sedimentary environmental conditions (Sibley & Gregg, 1987). The geochemical data and interpretations are described in detail below.

Strontium isotope

Description. The Sr isotope ratio (^{87}Sr/^{86}Sr) of the three types of dolostones ranges from 0.704528 to 0.705372 (average = 0.705006; Table 3). In detail, the ^{87}Sr/^{86}Sr values of the three types of dolostone have discrete ranges

(Fig. 7). The values of Type II dolostones have a narrow range of 0.704528 to 0.704986 (average = 0.704829) which is the lowest among the three types of dolostones. In contrast, the value of Type I dolostone has the greatest range (0.705137 to 0.705327, average = 0.705218). Finally, the $^{87}Sr/^{86}Sr$ value of Type III dolostones (0.704829 to 0.705030, average = 0.704932) falls between those of types I and II dolostones.

Interpretation. The data points of three types of dolostones (Fig. 7) are clustered between the range of global marine Permian carbonate (0.7067 to 0.7085; Burke *et al.*, 1982) and the global average of mantle-derived rocks (0.7035; Palmer & Elderfield, 1985), and is much lower than the range of crustal salic rocks (0.720 ± 0.005; Faure, 1986). This pattern indicates that the fluid from which dolomite was precipitated was predominantly from a deep source. The deeply sourced fluid probably evolved through water–rock reactions during upward migration, and eventually mixed with the lake water. The values of Type II dolostone indicate that the precipitating fluid of Type II dolostone was derived from the mantle with little crustal contamination. This interpretation is consistent with the presence of only pyroclastic vitric and crystal grains in this type (Fig. 4). The range of Type I suggests a significant contamination of mantle-derived fluid by crustal materials, which is consistent with the presence of terrigenous grains in this type (Fig. 3). The value of Type III dolostones can be explained by the high content of pyroclastic grains and alteration by acidic fluids.

Magnesium isotope

Description. $\delta^{26}Mg$ values of all three types of dolostones exhibit a relatively narrow range from −0.89 to −0.24‰ (average = −0.55‰; Table 3). In detail, $\delta^{26}Mg$ values of Type II dolostones have a narrow range and a heavy average value (−0.63 to −0.33‰, average = −0.42‰). On the other hand, types I and III dolostones are −0.89 to −0.24‰, and −0.86 to −0.39‰, respectively.

Interpretation. The range of the three types of dolostones is close to that of fresh middle oceanic ridge basalt (−0.25 ± 0.07‰) but very different from that of most of reported dolostones (Fig. 8; Teng, 2017). The narrow range and heavy value of Type II dolostones indicate a close affinity with a mantle-derived fluid, whereas the relatively broad ranges of types I and III dolostones suggests increased fractionation of Mg isotopes, which was probably caused by a mixed mantle and terrigenous source and/or reactions with acidic fluid. This interpretation is consistent with the results reported by Huang *et al.* (2015) and Geske *et al.* (2015a,b) that Mg isotopic fractionation is controlled by complex kinetics in precursor formation, diagenetic reaction and variable Mg source mixing.

Carbon and oxygen isotopes

Description. Overall, the $\delta^{13}C$ values of the three types of dolostones are positive (3.7 to 9.9‰, average = 5.6‰; Table 3) and the $\delta^{18}O$ values are negative (−22.7 to −3.1‰, average = −14‰). In detail, types I and II dolostones have a similar range of positive $\delta^{13}C$ values of 5.2 to 9.9‰ (average = 6.9‰) and 5.6 to 7.1‰ (average = 6.3‰) respectively, which are much higher than that of Type III dolostones (3.7 to 5.0‰, average = 4.3‰). On the other hand, types II and III dolostones, which contain common pyroclastic grains, have negative $\delta^{18}O$ values ranging from −17.4 to −13.7‰ (average = −15.4‰) and −22.7 to −17.1‰ (average = −20.7‰), respectively. Type I dolostones containing volcanic and terrigenous grains have the least negative $\delta^{18}O$ (−6.1 to −3.1‰; average = −4.3‰) values.

Interpretation. The range of $\delta^{13}C$ values is similar to that of methanogenetic dolomite and authigenic carbonates in alkaline lakes, indicating influence of microbial activities (Fig. 9; Mazzullo, 2000; Roberts *et al.*, 2004; Wacey *et al.*, 2007; Kenward *et al.*, 2009) and/or evaporation (Talbot & Kelts, 1990; Liu *et al.*, 2001; Cangemi *et al.*, 2016; Newell *et al.*, 2017). However, the range of $\delta^{18}O$ values is similar to that of hydrothermally altered dolomite (Davies & Smith Jr., 2006; Lonnee & Machel, 2006; Hollis *et al.*, 2017). Furthermore, both $\delta^{13}C$ and $\delta^{18}O$ values differ significantly from that of sulphate reduction dolomite in subtidal and peritidal environments (Mazzullo, 2000).

Generally, positive C isotopes can be explained by several factors, such as methanogenesis, high primary organic productivity and isotopically positive C inorganic sources (Mazzullo, 2000; Liu *et al.*, 2001; Roberts *et al.*, 2004; Wacey *et al.*, 2007; Kenward *et al.*, 2009; Hollis *et al.*, 2017; Newell *et al.*, 2017; Yang *et al.*, 2021). Combined with the observation of mantle source materials supported by Sr and Mg isotopes, abundant microbial deposits, as well

Table 2. Petrological features of Type III smectite-rich dolostone from the Lucaogou Formation, Santanghu Basin.

	Mineral compositions (wt. %)*							Sedimentary structure		Dolomite texture		
Sample No.	D	P	K	Q	C	S	Pr	Thickness (cm)	Geometry	Size (μm)†	Shape‡	Order degree
L-1	65.3	2.5	3.4	0	0	28.8	0	3	Massive Crudely laminated	10–35, 5–25	Subeuhedral–anhedral Anhedral	0.55
L-2	64.8	0.7	2.3	0	0	32.2	0	5	Massive Soft deformation	15–40, 10–30	Euhedral–subeuhedral Anhedral	0.48
L-3	51.9	0.8	1.3	0	0	43.5	2.5	6	Massive Crudely laminated	15–35, 20–30	Subeuhedral–anhedral Anhedral	0.35
L-5	57.8	0.5	1.1	0	0	40.4	0.2	8	Massive	20–50, 5–25	Euhedral–subeuhedral Anhedral	0.65
L-7	73.3	2.9	3.1	0	0	20.1	0.6	3	Massive Crudely laminated	10–35, 5–30	Subeuhedral–anhedral Anhedral	0.42
L-8	56.8	0.2	0.7	0	0	41.4	0.9	4	Massive	20–40, 5–25	Euhedral–subeuhedral Anhedral	0.45
L-12	53.4	6.8	12.5	0	0	26.1	1.2	5	Massive Crudely laminated	20–30, 5–30	Subeuhedral–anhedral Anhedral	0.54
L-14	52.3	0.4	3.2	0	0	42.8	1.3	7	Massive	10–50, 5–25	Euhedral–subeuhedral Anhedral	0.56

* The mineral compositions of dolostone and the order degree of dolomite are determined by X-ray diffraction (XRD). D – dolomite, P – plagioclase, K – K-feldspar, Q – quartz, C – calcite, S – smectite, Pr – pyrite. † The left part is the size of dolomite in aggregate, whereas the right part is dolomite in matrix. ‡ The upper part is the shape of dolomite in aggregate, whereas the lower part is dolomite in matrix.

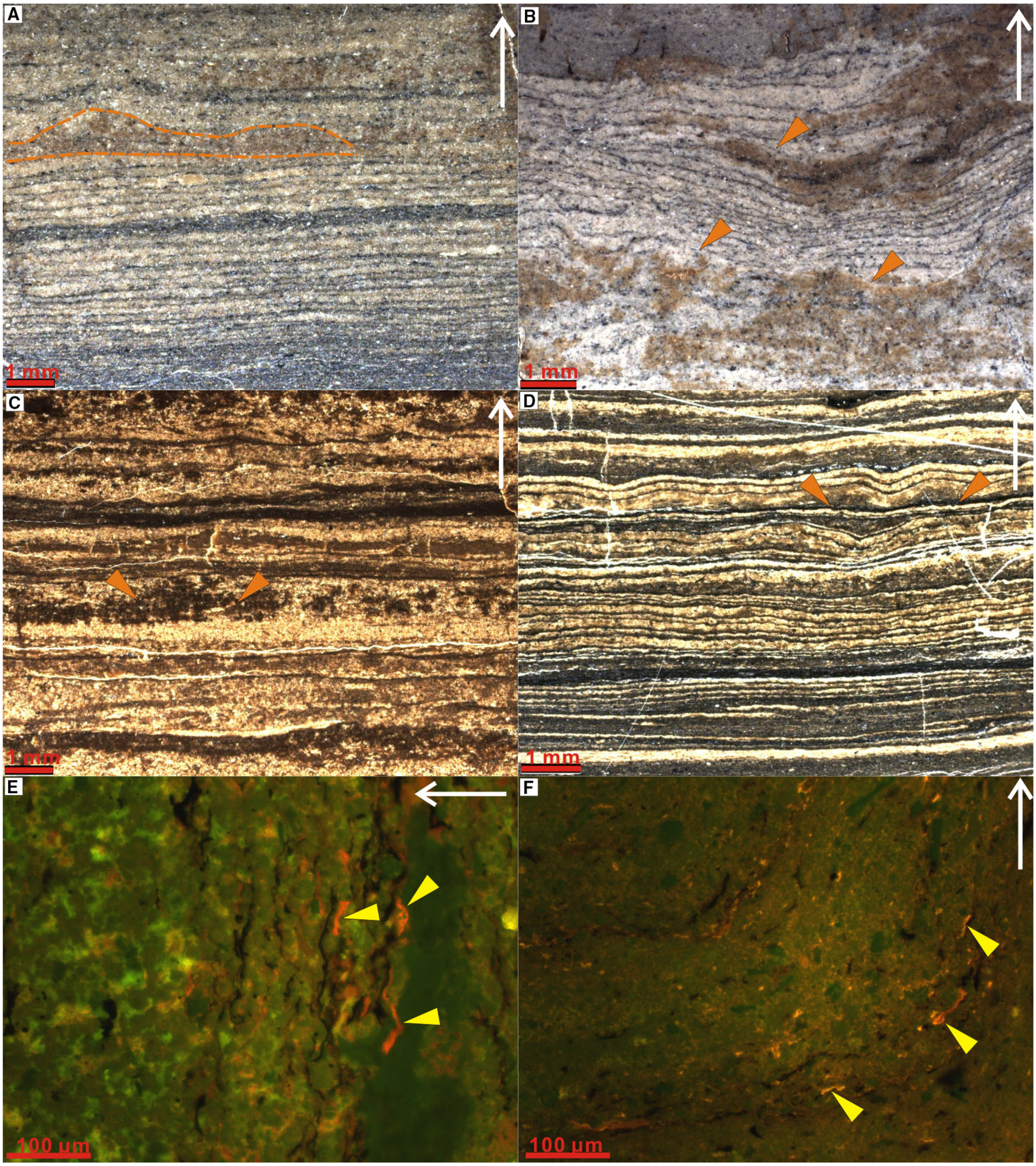

Fig. 6. Photomicrographs showing microbial laminations and build-ups in types I and II dolostones. (A) to (D) were taken under a stereomicroscope; (E) and (F) are under incident blue light illumination. Exposure time is 3 s. The white arrows show the stratigraphic-up direction. (A) Bright brown dolostones interlaminated with dark grey to dark brown organic-rich laminae. The grey laminae are subparallel and crenulated, indicating microbial (algal) laminations. Some cone-shaped bodies with a flat base and a convex top are relatively rich in organic matter (orange dashed lines), suggesting microbial build-ups. Sample N-11. (B) Dolostones interlaminated with organic-rich laminae with soft-sediment deformation. Some microbial build-ups (orange arrows) are present. Sample N-5. (C) Common organic-rich microbial build-ups (orange arrows) in laminated dolostones. Sample N-15. (D) The same as (C) Sample M-3. (E) Common orange-coloured alginate (yellow arrows) in organic-rich laminae. Sample N-3. (F) Common orange-coloured alginate (yellow arrows) in soft-sediment deformed organic-rich laminae. Sample M-3.

Table 3. Mg istotopic compositions, $^{87}Sr/^{86}Sr$ ratios, δ ^{13}C and δ ^{18}O values for dolostones from the Lucaogou Formation, Santanghu Basin.

Sample No.	$\delta^{25}Mg \pm 2SD^*$ (‰)	$\delta^{26}Mg \pm 2SD$ (‰)	$(^{87}Sr/^{86}Sr)_0\dagger \pm 2SD$	$(^{87}Sr/^{86}Sr)_i\ddagger$	$\delta^{13}C$ (‰)	$\delta^{18}O$ (‰)
N-2	−0.46 ± 0.03	−0.89 ± 0.07	0.705194 ± 0.000006	0.705194	5.6	−3.4
N-3	−0.30 ± 0.05	−0.55 ± 0.04	0.705190 ± 0.000005	0.705137	6.4	−4
N-5	−0.35 ± 0.03	−0.67 ± 0.09	0.705270 ± 0.000009	0.705207	5.2	−5.2
N-11	−0.28 ± 0.06	−0.43 ± 0.05	0.705383 ± 0.000006	0.705327	7.6	−6.1
N-15	−0.09 ± 0.04	−0.24 ± 0.01	0.705316 ± 0.000007	0.705278	9.9	−3.1
N-24	−0.40 ± 0.04	−0.74 ± 0.06	0.705307 ± 0.000007	0.705163	6.4	−3.7
M-3	−0.22 ± 0.02	−0.40 ± 0.03	0.704984 ± 0.000004	0.704952	6.7	−13.9
M-2	−0.14 ± 0.06	−0.33 ± 0.05	0.705020 ± 0.000006	0.704986	7.1	−13.7
M-1	−0.17 ± 0.04	−0.33 ± 0.08	0.704665 ± 0.000006	0.704528	5.6	−16.4
M-8	−0.34 ± 0.04	−0.63 ± 0.04	0.704922 ± 0.000005	0.704851	5.6	−17.4
L-1	−0.30 ± 0.03	−0.61 ± 0.06	0.705237 ± 0.000008	0.704963	3.8	−21.2
L-2	−0.26 ± 0.01	−0.50 ± 0.07	0.705255 ± 0.000012	0.704913	5.0	−17.9
L-3	−0.37 ± 0.03	−0.72 ± 0.06	0.705309 ± 0.000006	0.704960	4.7	−17.1
L-5	−0.28 ± 0.06	−0.55 ± 0.01	0.705788 ± 0.000009	0.704958	4.9	−21.8
L-7	−0.24 ± 0.02	−0.46 ± 0.07	0.705058 ± 0.000010	0.704936	4.6	−21.8
L-8	−0.56 ± 0.01	−0.62 ± 0.04	0.705201 ± 0.000015	0.705030	4.2	−22.7
L-12	−0.45 ± 0.05	−0.86 ± 0.08	0.705382 ± 0.000009	0.704866	3.7	−22.1
L-14	−0.22 ± 0.01	−0.39 ± 0.05	0.705262 ± 0.000009	0.704829	3.8	−21.0

* 2SD = two times the standard deviation of the population of n ($n > 3$) repeat measurements of the standards during an analytical session. † $(^{87}Sr/^{86}Sr)_0$ is the testing ratio. $(^{87}Sr/^{86}Sr)_i$ is the calculated initial ratio. ‡ $(^{87}Sr/^{86}Sr)_i = (^{87}Sr/^{86}Sr)_0 - {^{87}Rb}/{^{86}Sr} \times (e^{\lambda t} - 1)$. $\lambda = 1.42 \times 10^{-11}$; t = 270 Ma; e = 2.718.

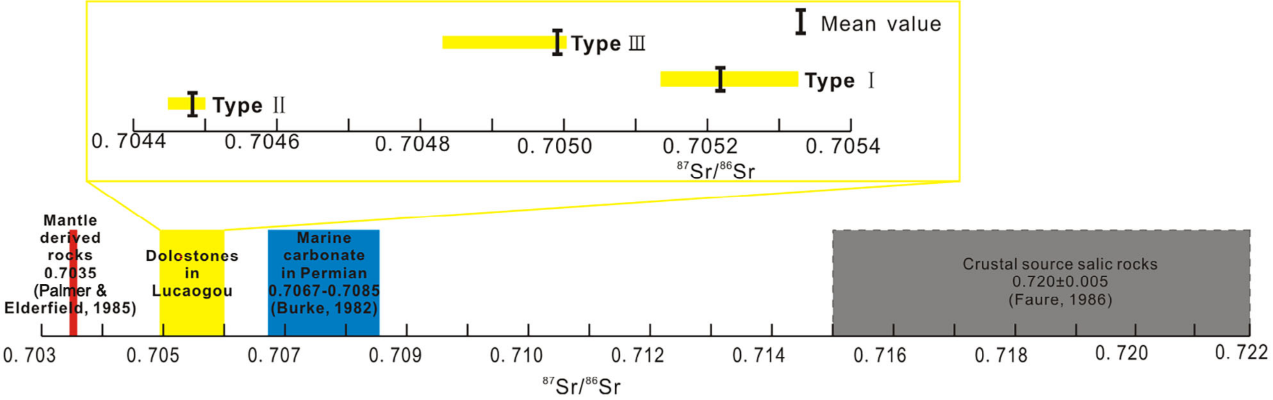

Fig. 7. Diagram showing the range of Sr isotope ratio of dolostones in the Lucaogou Formation and other common rock sources from Palmer & Elderfield (1985), Burke *et al.* (1982) and Faure (1986).

as organic-rich lamination in types I and II dolostones (see *Geochemical characteristics of dolostones*), it is speculated that the formation of dolomite in those dolostones was influenced by isotopically positive C inorganic sources, and/or modified by microbial activities of methanogenesis (Mazzullo, 2000). Firstly, the volcanic activities not only provide clastics, but also release a huge amount of volatiles including CO_2 (Lilley *et al.*, 2003), causing the release of lighter ^{12}C. As a result, the heavier ^{13}C was precipitated in the dolomite (Lilley *et al.*, 2003; Kele *et al.*, 2008; Yang *et al.*, 2021). Second, Type III dolostones, which contain a rare microbial deposit with organic fragments (Fig. 5D, E and G), also have abundant microcrystalline dolomite. The direct relationship of microbial activities on dolomite formation is not evident in this study. Hence, it is speculated that the nucleation of dolomite in the three types of dolostones were not strongly influenced by microbial activities. However, types I and II dolostones were likely influenced during burial by methanogenesis, which may have caused the positive $\delta^{13}C$ values.

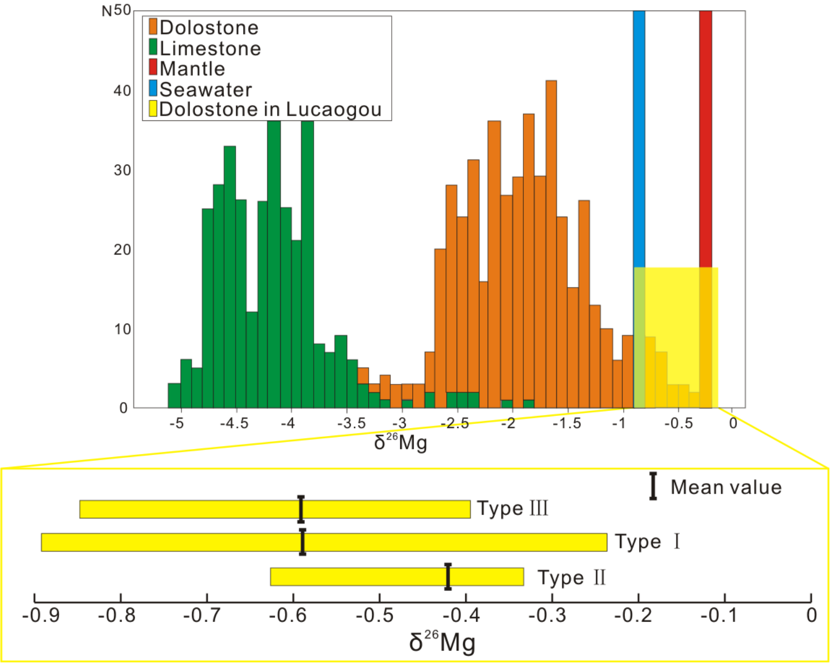

Fig. 8. Diagram showing the range and distribution of Mg isotope composition of dolostones in the Lucaogou Formation of the Santanghu Basin. The Mg isotopic data are from Teng (2017), who summarized dolostone samples from various geological settings, including biogenic and abiogenetic, as well as lacustrine and marine dolostones.

Commonly, the negative $\delta^{18}O$ values of dolostones suggest possible influence of freshwater or hydrothermal fluids (Boni *et al.*, 2000; Davies & Smith Jr., 2006; Hollis *et al.*, 2017). During evaporation, light ^{16}O is preferentially removed to cause enrichment of ^{18}O in carbonate minerals (Talbot & Kelts, 1990; Liu *et al.*, 2001). Thus, the relatively negative $\delta^{18}O$ values suggest that the volcanism-related hydrothermal fluids had significantly influenced the dolomite formation. This is supported by the abundance of pyroclastic grains, rarity of terrigenous grains and lack of evaporitic features in the three types of dolostones. Furthermore, generally, a prolonged and/or strong hydrothermal presence will cause more negative $\delta^{18}O$ values. For example, for a well-crystallized and altered hydrothermal saddle dolomite, its $\delta^{18}O$ value is more negative than a later altered hydrothermal dolomite without saddle texture (Lonnee & Machel, 2006; Hollis *et al.*, 2017; Fig. 9). This tendency coincides with the characteristic $\delta^{18}O$ values of the three types of dolostone. In other words, types II and III dolostones with abundant pyroclastic grains have much lower $\delta^{18}O$ values than that of Type I dolostones containing volcanic and terrigenous grains. Above all, the formation of the dolomite in this study was strongly influenced by volcanic–hydrothermal fluid.

Major, trace and rare earth elemental composition

Description. The Mg/Ca ratio of all three types of dolostone ranges from 0.36 to 0.69 (average = 0.56; Table S1) and is consistent with their low degree of cation ordering. The distribution of major elements in the dolomite crystals in the dolostones is uniform without zonation under cathodoluminescence (CL) and microprobe (Figs 3F, 4G, 5D and 5G). Type II dolostone has the highest FeO content with an average of 7.84%, in comparison to 0.72% and 1.33% for types I and III dolostones, respectively. The total REE content (∑REE) of the three types of dolostones ranges from 11.73 to 142.88 ppm, (average = 49.89 ppm; Table S2). The REE pattern was normalized to the North American Shale Composite (NASC; Fig. 10A) and Primitive Mantle (PM; Fig. 10B) for comparative study. For the NASC, the pattern is slightly flattened with a weakly negative trend (δCe* ranging from 0.87 to 0.94, average = 0.9), whereas the pattern shows a clear Eu negative anomaly (δEu* ranging from 0.49 to 0.90, average = 0.68) for the PM.

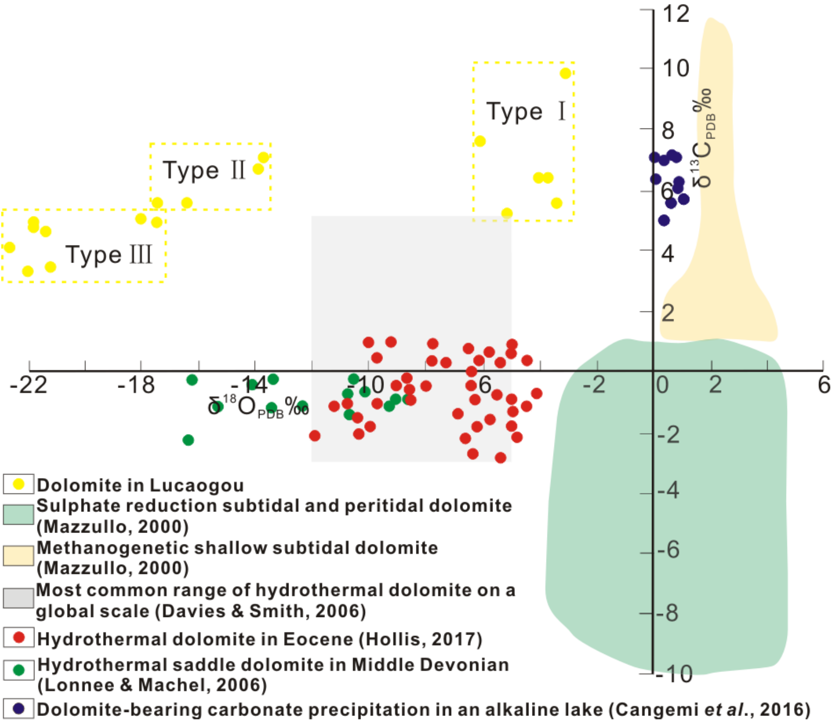

Fig. 9. Plot of stable carbon and oxygen isotope values of dolostones in the Lucaogou Formation. Typical ranges of other dolostones are from Mazzullo (2000), Davies & Smith Jr. (2006), Lonnee & Machel (2006), Cangemi *et al.* (2016), Newell *et al.* (2017) and Hollis *et al.* (2017).

Interpretation. The highest Fe concentration of Type II dolostone is consistent with the most abundant pyroclastic grains, indicating that the Fe concentration is the highest in the primary dolomite-precipitating fluid. The ∑REE of the three dolostones is very different from that of hydrothermally altered dolostone (for example, 0.82 ppm on average; Hollis *et al.*, 2017). However, the content is close to that of tuffaceous shale (96 ppm) and middle Permian basalt (109.5 ppm) in the Santanghu Basin (Zhao *et al.*, 2006) because of the incorporation of pyroclastic grains in dolostones. In other words, Type I pyroclastic-poor dolostones have the lowest value (average = 37.13 ppm), followed by Type III (average = 51.70 ppm) and Type II (average = 66.32 ppm). Those features indicate a close relationship between dolostone formation and volcanism.

The NASC REE pattern is different from that of hydrothermally altered dolostones, which have an apparent negative Ce, positive La and slightly flattened HREE (Hollis *et al.*, 2017). In addition, the pattern of the three types of dolostones shows nearly the same features with that of tuffaceous shale, and a similar trend to that of middle Permian basalt (Fig. 10). In addition, the PM REE pattern is similar to that of the carbonates with volcanic deposits in a distal (up to 400 m) hydrothermal zone of volcanic massive sulphide (VMS) hydrothermal systems (Genna *et al.*, 2014). The Ce pattern shows no anomaly and is different from that of deposits in the typical volcanic–hydrothermally-influenced alkaline Lake Van in Italy (Möller & Bau, 1993).

Furthermore, some trace elements are widely used to reflect the lacustrine environments during the nucleation of dolomite. Firstly, a Y/Ho ratio greater than 28 generally reflects marine water invasion or saline lake water (Lawrence & Kamber, 2006; Cao *et al.*, 2020). The range of Y/Ho ratios of the three types of dolostones is 27.44 to 30.57, (average = 28.70; Table S2), indicating that dolostones were formed in saline water. In addition, U, Th, V, Ni and Cr are used to evaluate the redox state. For example, the ranges of $U/Th > 1.25$, $1.25 > U/Th > 0.75$ and $U/Th < 0.75$ reflect anoxic, dysoxic and oxic environments, respectively (Cao *et al.*, 2020). The values of $V/(V + Ni) > 0.45$ and $V/Cr > 2$ indicates anoxic environments (Jones & Manning, 1994; Cao *et al.*, 2020). The range of U/Th

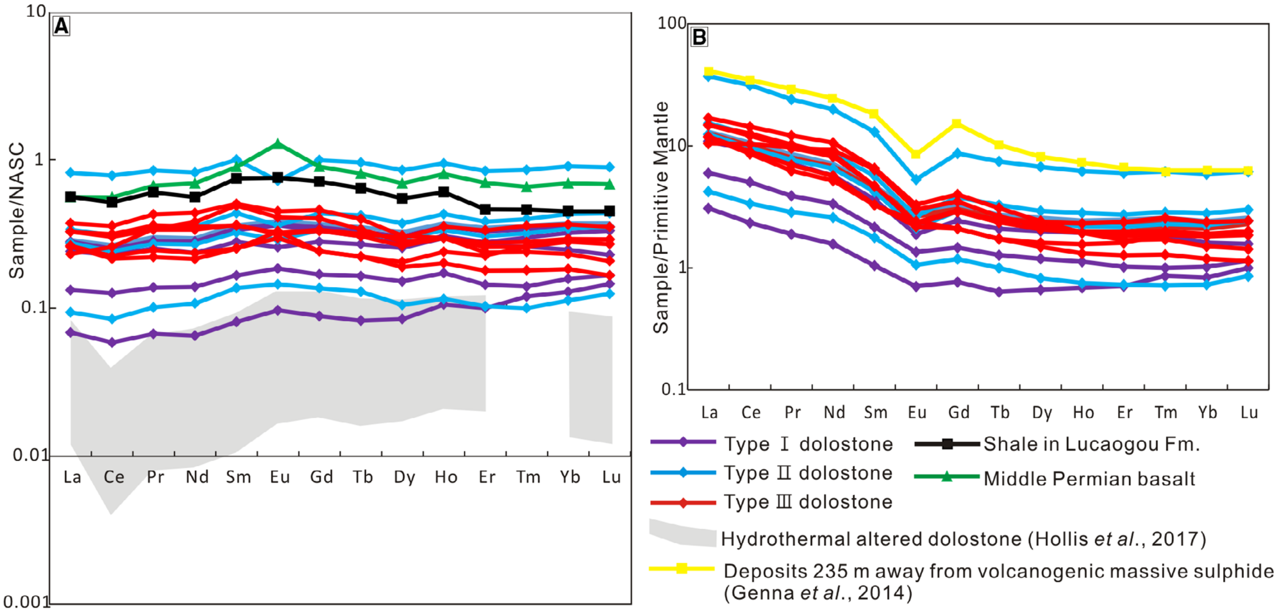

Fig. 10. Rare earth element (REE) pattern of dolostones. (A) REE patterns of all three types of dolostones normalized to the North American Shale Composite (NASC; Gromet *et al.*, 1984), hydrothermally altered dolostone (Hollis *et al.*, 2017) and shale in the Lucaogou Formation and middle Permian basalt in the Santanghu Basin (Zhao *et al.*, 2006). (B) REE patterns of all three types of dolostones normalized to PM (Sun & McDonough, 1989) and of deposits 235 m away from volcanogenic massive sulphides (Genna *et al.*, 2014).

ratios of the three types of dolostones is 0.32 to 1.55 (average = 0.88); that of V/(V + Ni) is 0.68 to 0.93 (average = 0.84); that of V/Cr is 1.7 to 6.88 (average = 4.27). The range of ratios for U/Th indicates a dysoxic environment, while the ranges of other ratios indicate an anoxic environment.

DISCUSSION

Depositional environments of dolomite

The sedimentary structures, mineral compositions and textures of the studied dolostones and adjacent tuffaceous shale in the Lucaogou Formation indicate a subaqueous lacustrine environment controlled by volcanic–hydrothermal activities. The low cation ordering (average = 0.45; Tables 1 and 2), euhedral crystal form (Figs 3G and 4C), and nano-sizes to micron-sizes of dolomite in all three types of dolostones are consistent with those of protodolomite in Holocene deposits reported by Graf & Goldsmith (1956) and Gregg *et al.* (2015). In addition, four characteristics of the dolomites indicate their syndepositional primary origin, as defined by Sibley & Gregg (1987). They include: (i) very fine laminations with little soft-sediment deformation (Figs 3 and 4); (ii) homogeneous nucleation, as suggested by uniformly distributed nano-sized to micron-sized crystals without zonation, indicating weak diagenetic alteration (Figs 3F, 4F, 5D and 5G); (iii) well-preserved fabric (Figs 6 and S3); and (iv) absence of microcrystalline calcite and aragonite. Modern and Neogene microcrystalline dolomites occur mainly in high-salinity environments, such as sabkha flats, hypersaline lagoons and playa lakes, where evaporation is intense (Arvidson & MacKenzie, 1999; Petrash *et al.*, 2017). However, the Lucaogou dolostones do not contain any evaporite minerals and their pseudomorphs, as well as evaporitic sedimentary structures, such as dewatering-induced shrinkage cracks and subaerially exposed and transported sediments with ripple marks (Alsharhan & Kendall, 2003; Garcia-Fresca *et al.*, 2018; Guo *et al.*, 2021).

On the contrary, many lines of evidence from the Lucaogou dolostones suggest a subaqueous environment with frequent and abundant influx of volcanic and hydrothermal materials. Recent studies on the mineralogy and elemental geochemistry of the dolostones and tuffaceous shales in the Lucaogou Formation interpreted an anoxic and saline lake environment with abundant synsedimentary volcanic ash and hydrothermal deposits (Jiao *et al.*, 2020; Liu *et al.*, 2020; Pan *et al.*, 2020; Zhang *et al.*, 2021). In this study, the trace elemental compositions of the three types of dolostones also indicate a saline and anoxic environment. The Lucaogou sediments are sandwiched by alkaline basalts (Figs 2 and S1; Wang *et al.*, 2015; Zhou *et al.*, 2006). The well-developed build-ups of volcanic–hydrothermal deposits (Fig. S2; see details in Jiao *et al.*, 2018a,b) and basalts in the Lucaogou Formation indicate active volcanism, albeit subdued in comparison to the subjacent and suprajacent formations. In addition, the dolostones are interlaminated with tuffaceous shales, indicating frequent volcanism in Lucaogou lake (Jiao *et al.*, 2020). The same REE pattern (Fig. 10) as that of the distal VMS deposits further supports this interpretation. The distal zone is characterized by the destruction of volcanic glass leading to a negative Eu anomaly at the early and relatively low temperature environment (Genna *et al.*, 2014). This interpretation is supported by the close spatial relationship between the distribution of dolostones and volcanic centres in study area (Fig. 1C) as well as the weakly altered volcanic glass in samples from the study.

Furthermore, the Sr, Mg and O isotope values (Figs 7 to 9) indicate that the dolomite-precipitating fluid has similar isotopic compositions to those of mantle-derived hydrothermal fluids (see *Geochemical characteristics of dolostones*). In addition, the low clay content of the Lucaogou dolostones (Table 2) and adjacent tuffaceous shales (Hackley *et al.*, 2016; Jiao *et al.*, 2020) indicates a closed lake with limited terrigenous detrital influx (e.g. Boak & Poole, 2015). All of the above evidence indicates a high-salinity Lucaogou lake, which is characterized by dolomite precipitation, influx of volcanic–hydrothermal materials and intense microbial activities in a closed saline environment in a tectonically active volcanic setting. Lucaogou lake is likely similar to modern lakes, such as Lake Magadi and Lake Bogoria in the East African Rift Zone, and Mono, Albert, Goodenough and Last Chance lakes in North America (Pecoraino *et al.*, 2015; Cao *et al.*, 2020).

However, Lucaogou lake has some unique features that are very different from evaporitic mixed volcanic–hydrothermal alkaline lakes (Pecoraino *et al.*, 2015; Cao *et al.*, 2020), where evaporation is the main cause for high alkalinity and salinity (Stüeken *et al.*, 2015). The absence of highly alkaline minerals, evaporitic sedimentary structures and the normal δCe value all indicate weak evaporation. Hence, Lucaogou lake is just locally alkaline or weakly alkaline and, thus, conducive to dolomite formation. It is in contrast to the highly alkaline lake of the Permian Fengcheng Formation in the Junggar Basin (Cao *et al.*, 2020).

Factors and processes promoting primary dolomite formation

Hydrothermal fluid provides materials and a relatively high temperature and can directly or indirectly cause microcrystalline dolomite formation. Volcanic lakes undergo a period of active eruptive accumulation of volcaniclastic sediments, which is followed by a period of slow settlement of suspension load under relatively stable lake conditions. The lake may also be influenced by volcanism-related sublacustrine hydrothermal systems to form sediment-hosted geothermal systems (Fisher, 1984; White, 2000; Pittari *et al.*, 2016; Procesi *et al.*, 2019). In this unique environment, deposition of sediments from volcanic, hydrothermal, lacustrine and terrigenous sources are complex. Two major factors and processes may cause microcrystalline dolomite formation and are discussed in detail below.

Firstly, a relatively high temperature of the bottom water on the lake floor may promote dolomite nucleation. Laboratory experiments show that the imperfectly ordered to ordered dolomite can precipitate at *ca* 50°C (Arvidson & MacKenzie, 1999). Unfortunately, the Lucaogou dolomite crystals are too small to be used to measure the homogenization temperature of fluid inclusions in order to estimate the dolomite nucleation temperature. However, a broad temperature range of dolomite nucleation can be estimated. The lower limit of the range should be higher than the temperature of the ambient lake water. This is interpreted from the negative $\delta^{18}O$ values of dolostones, which suggest the influence of hydrothermal fluids during dolomite formation (see section on *Carbon and oxygen isotopes*). It is reasonable to speculate that the hydrothermal fluids would have a higher temperature than the ambient lake water. The upper limit can be regarded as the homogenization temperature obtained from inclusions in well-crystallized dolomite in the soft-sediment deformation and fluid escape structures in Type III dolostone and is *ca* 86°C (Fig. S5). The data indicates a relatively high temperature of pore water at the very early stage of burial before lithification.

Second, the bottom water of Lucaogou lake was likely saturated with Mg and Ca, which is critical to dolomite nucleation. This interpretation is based on modern analogues. In modern hydrothermal fields, many elements and gases, such as Mg, Ca, Fe, CO_2 and CH_4, which are not common in normal lake waters, are locally enriched through water–rock interaction or direct influx from the mantle (Kelley *et al.*, 2001; Procesi *et al.*, 2019). The dolostones in the study area are distributed around the volcanic centres (Figs 1C and 2). The basalts in the Lucaogou Formation (Fig. 2) and the thick mafic rocks in the subjacent formations may have supplied abundant Mg and Fe, as supported by the Sr and Mg isotope values (Figs 7 and 8). This fluid may have provided a large quantity of Mg for dolomite nucleation.

Model for dolostone formation in an alkaline volcanic lake

The distribution of the three types of Lucaogou dolostones forms a general pattern of gradual transition from the volcanic eruption centre to the distal field, corresponding mainly to gradual changes in lake water chemistry and temperature (Table 4; Fig. 11). The microcrystalline dolomite formed in a subaqueous intracontinental volcanic lake. The lake was strongly influenced by volcanic and hydrothermal activities (Fig. 11A). Two types of hydrothermal fluids occurred in this lake. The most important and abundant type is the mantle-derived hydrothermal fluid (magmatic water), as suggested by the Sr and Mg isotopes. The second type is the heated lake water, which seeped into underlying strata along fractures at the shallow depth and was heated by magma to generate pressurized steam that then welled up. The similar REE pattern with tuffaceous shale (Fig. 10) may support this speculation. Dolomite nucleation occurred directly under conditions controlled by two main factors. That is, the volcanic–hydrothermally-induced local environment had a relatively high temperature and continuous supply of Mg and Ca, both of which induced a high-salinity and anoxic lake bottom environment, which was conducive to dolomite nucleation (Arvidson & MacKenzie, 1999; Yang *et al.*, 2020, 2021). In this unique environment, the emission and flow of hydrothermal fluid away from the volcanic centre determined that the three types of dolomitic sediment were systematically deposited and distributed in separate areas in relation to the distance from the centres of volcanic–hydrothermal activities (Fig. 11A). Where the hydrothermal fluids and lake waters mixed far away from the volcanic centres, dolomite nucleated *in situ* and incorporated scarce terrigenous and pyroclastic grains settled from the water column to form well-laminated and lamalginite-rich Type I pyroclastic-poor dolostone (Fig. 11B). This interpretation is also supported by the highest $^{87}Sr/^{86}Sr$ ratio and $\delta^{18}O$ value, and low $\delta^{26}Mg$ value (Table 4; Figs 7 to 9) of Type I dolostone. In the hydrothermal and volcanic mixed field, dolomite mixed with abundant pyroclastics to form well-laminated and lamalginite-rich Type II dolostones (Fig. 11C). The sediments were likely soft-sediment deformed due to the relative closeness to the volcanic–hydrothermal centres. Thus, the dolomite-precipitating water is mainly composed of hydrothermal fluid, which is characterized by the lowest $^{87}Sr/^{86}Sr$ ratio, moderately negative $\delta^{18}O$ value and largest $\delta^{26}Mg$ value (Figs 7 to 9). In the area on or in the vicinity of the volcanic–hydrothermal centres, the freshly precipitated unsolidified dolomite sediments would be greatly disturbed and intensively mixed with volcanic ash to form sediment gravity flows which deposited the massive and thin-bedded Type III smectite-rich dolostones (Fig. 10D). As a result, abundant volcanic ash-altered smectite occurs in this type of dolostone. The complex nature of the mixed water of Type III dolostones is indicated by its moderately $^{87}Sr/^{86}Sr$ ratio, lowest $\delta^{18}O$ value and low $\delta^{26}Mg$ value (Figs 7 to 9). It is evident that the ranges of Sr, O and Mg isotopic values of types I and III dolostones are much wider than those of Type II dolostones. The difference indicates that the dolomite precipitating waters of types I and III dolostones have a complex origin and/or have experienced strong isotopic fractionation.

Finally, frequent volcanism–hydrothermal activities also provided copious nutrients in the sediment and water for intense microbial activities (Xie *et al.*, 2010; Zhang *et al.*, 2017), as indicated by the many alginites, microbial build-ups and microbial crusts in types I and II dolostones (Figs 6 and S7). The C isotopic composition of the dolostones is also influenced by methanogenesis during shallow burial (e.g. Mazzullo, 2000) to cause a positive anomaly. However, Type III dolostone was altered by acidic

Table 4. Main features of the three types of dolostones in the Lucaogou Formation, Santanghu Basin.

Types	Mineral compositions	Sedimentary structures	Organic matter	Isotopes	Interpreted
Type I	*Ca* 80% dolomite with 0.4 of cation ordering (Fig. 3G); shard-like pyroclastics and rounded terrigenous grains (Fig. 3E)	Laminated and intercalated within tuffaceous shale (Fig. 3C); non-dolomite grains are scattered discretely in dolostones without orientation (Fig. 3E)	Interlaminated with lamalginite, abundant microbial build-ups (Fig. 6A, B, C and E) and microbial crust (Fig. S7)	Sr: highest ratio with broad range; Mg: lighter value with broad range; C and O: heaviest C and O values	Predominantly dolomite formed *in situ* and mixed with minor suspension settling terrigenous and pyroclastic grains in a quiescent subaqueous environment
Type II	*Ca* 77% dolomite with 0.4 of cation ordering (Fig. 4C); predominantly shard-like vitric and crystal grains (Fig. 4E, G and H)	Mainly laminated with soft-sediment deformation (Fig. 4A) to minor thin bed (Fig. 4B); intercalated within tuffaceous shale (Fig. 4B); pyroclastic grains accumulate close to lamalginite in laminated dolostone (Fig. 4D) and are scattered discretely in thin bed dolostone without orientation (Fig. 4G)	Interlaminated with lamalginite, abundant microbial build-ups (Fig. 6D and F) and microbial crust (Fig. S7)	Sr: lowest ratio with narrow range; Mg: heaviest value with narrow range; C and O: heavier C and lighter O values	Dolomite precipitated *in situ* mixed with suspension settling vitric-crystal grains in a relatively quiescent to locally turbulent subaqueous environment
Type III	Mainly *ca* 60% dolomite with 0.5 of cation ordering and *ca* 3% smectite (Fig. 5)	Thin to medium beds with massive and 'porphyritic' inner structures (Fig. 5A and B); aggregation of euhedral dolomite and smectite (Fig. 5D); minor occurrence of soft-sediment deformation and fluid escape structures (Fig. 5B); and dolomites in them are recrystallized and replaced by serpentine (Fig. 5F and G)	Minor occurrence of organic fragment (Fig. 5D, E and G)	Sr: medium ration with broad range; Mg: lightest value with broad range; C and O: lightest C and O values	Reworked by volcanic subaqueous eruption before dolomite crystals solidified

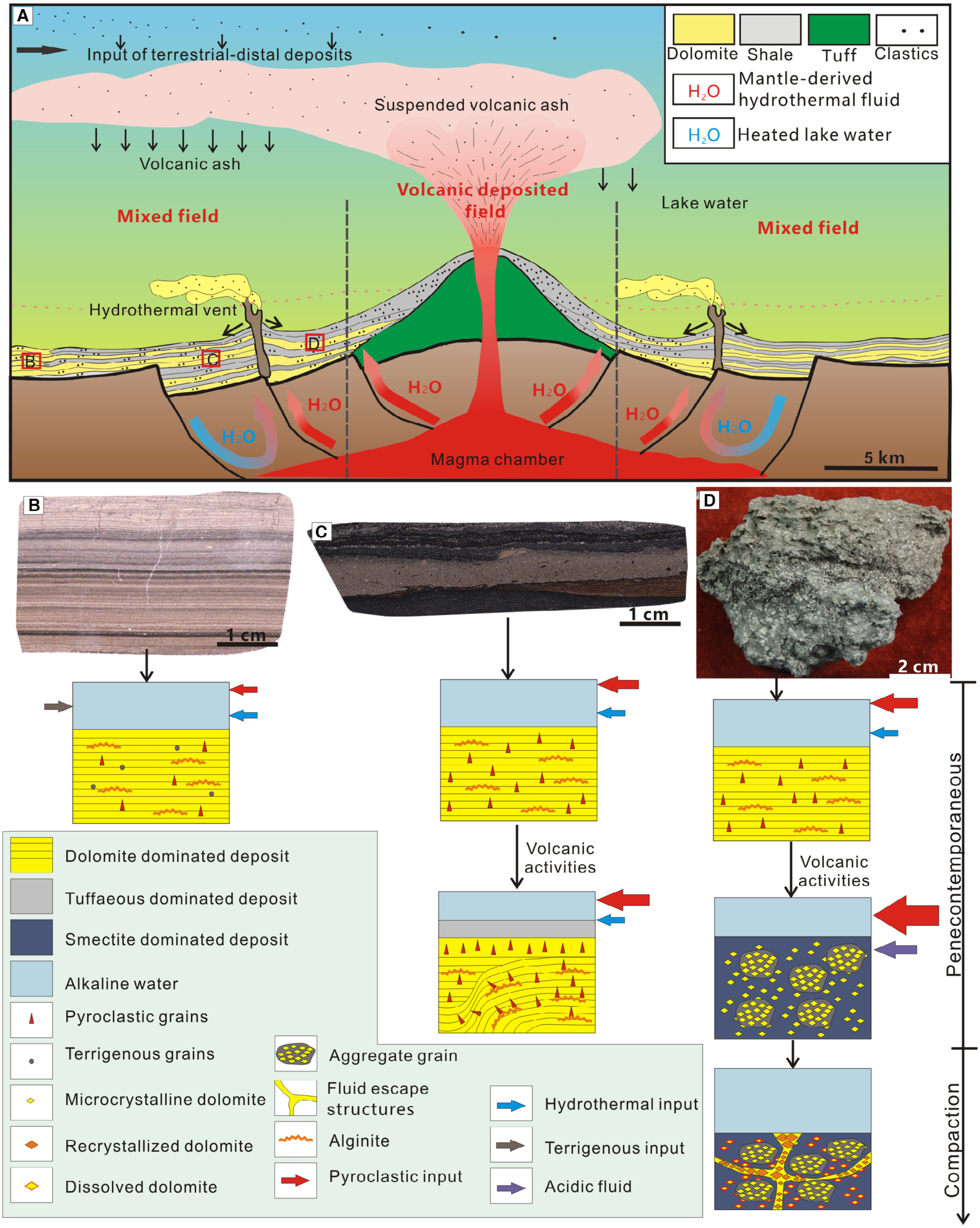

Fig. 11. Depositional model for the three types of Lucaogou dolostones in a volcanic lake. (A) The volcanic–hydrothermal lacustrine sedimentary environment, modified after Jiao *et al.* (2020). The scale is estimated on the basis of the distance between the volcanic centres and dolostone deposits on seismic sections. Red boxes are the locations of (B) to (D) which represent interpreted processes in the formation of Type I pyroclastic-poor, Type II vitric and crystal-rich and Type III smectite-rich dolostones, respectively.

fluids and transported by high-density flows, and was not influenced by microbial activities. As a result, Type III dolostone contains only a small amount of organic matter and does not show a significant positive C isotopic anomaly.

CONCLUSIONS

Detailed mineralogical, petrographic and isotopic geochemical data documented laminated dolostones in the middle Permian Lucaogou Formation of the Santanghu rift basin. A volcanic–hydrothermal lake is speculated to be the environment where microcrystalline dolomite precipitation occurred. In this environment, volcanic–hydrothermal activities generated favourable chemical conditions to promote dolomite precipitation. Multiple episodic volcanic eruptions and hydrothermal flows created chemical conditions with abundant Mg and Ca and raised the temperature on the lake floor so that the thermodynamic threshold for dolomite precipitation was reached.

This work provides a mechanism for the microcrystalline dolomite to precipitate directly in a subaqueous lacustrine environment influenced by volcanic–hydrothermal activities without evaporation. Most modern and Holocene microcrystalline dolomites have been studied in shallow water environments, where evaporation is commonplace. As a result, most ancient primary dolomite is interpreted as an evaporitic mineral formed in evaporitic environments. Findings in this study indicate that a continuous supply of Mg and Ca and a high temperature provided by subaqueous volcanic–hydrothermal activities can induce dolomite nucleation to form lacustrine dolostone. The Lucaogou dolostones provide an analogue for ancient massive primary dolomite formation without the commonly invoked processes of evaporation. Further research on primary dolomite formation in tectonically active sedimentary basins will expand the understanding of dolomite formation throughout geological history.

ACKNOWLEDGEMENTS

This work was supported by a grant from the National Science Foundation of China (41802120 to XJ) and a U.S. NSF grant (EAR 1714749 to WY). We are indebted to Professor Cathy Hollis, Associate Editor, and two anonymous reviewers who provided great insights and help on the science and writing that have significantly improved the manuscript. We thank Dr Kangjun Huang and Dr Wenlei Song in Northwest University for their help on analysis and commons of isotopic research.

DATA AVAILABILITY STATEMENT

The data that support the findings of this study are available from the corresponding author upon reasonable request.

REFERENCES

Alsharhan, A.S. and **Kendall, C.S.C.** (2003) Holocene coastal carbonates and evaporites of the southern Arabian gulf and their ancient analogues. *Earth-Sci. Rev.*, **61**, 191–243.

Arvidson, R.S. and **MacKenzie, F.T.** (1999) The dolomite problem: control of precipitation kinetics by temperature and saturation state. *Am. J. Sci.*, **299**, 257–288.

Boak, J. and **Poole, S.** (2015) Mineralogy of the Green River formation in the Piceance Creek basin, Colorado. In: *Stratigraphy and Paleolimnology of the Green River formation, Western USA* (Eds Smith, M. and Carroll, A.), syntheses in Limnogeology. 1, pp. 183–209. Springer, Dordrecht.

Boni, M., **Parentea, G.** and **Bechstadtb, T.** (2000) Hydrothermal dolomites in SW Sanlinia (Italy): evidence for a widespread late-Variscan fluid flow event. *Sed. Geol.*, **131**, 181–200.

Burke, W.H., **Denison, R.E.** and **Hetherington, E.A.** (1982) Variation of seawater ^{87}Sr/^{86}Sr throughout phanerozoic time. *Geology*, **10**, 516–519.

Cangemi, M., **Censi, P.**, **Reimer, A.**, **D'Alessandro, W.**, **Hause-Reitner, D.**, **Madonia, P.**, **Oliveri, Y.**, **Pecoraino, G.** and **Reitner, J.** (2016) Carbonate precipitation in the alkaline lake Specchio di venere (Pantelleria Island, Italy) and the possible role of microbial mats. *Appl. Geochem.*, **67**, 168–176.

Cao, J., **Xia, L.**, **Wang, T.**, **Zhi, D.**, **Tang, Y.** and **Li, W.** (2020) An alkaline lake in the late Paleozoic ice age (LPIA): a review and new insights into paleoenvironment and petroleum geology. *Earth-Sci. Rev.*, **202**, 103091.

Davies, G.R. and **Smith, L.B., Jr.** (2006) Structurally controlled hydrothermal dolomite reservoir facies: an overview. *AAPG Bull.*, **90**, 1641–1690.

Eickmann, B., **Bach, W.**, **Rosner, M.** and **Peckmann, J.** (2009) Geochemical constraints on the modes of carbonate precipitation in peridotites from the Logatchev hydrothermal vent field and Gakkel ridge. *Chem. Geol.*, **268**, 97–106.

Faure, G.P. (1986) *Principles of Isotope Geology*, 2nd edn, pp. 160–230. JohnWiley and Sons, New York.

Feng, Q., **Liu, Y.** and **Hao, J.** (2004) The source rock and its palaeo-environment of lucaogou formation permian in santanghu basin. *Acta Sedimentol. Sinica*, **22**, 513–517 (in Chinese with English abstract).

Fisher, R.V. (1984) Submarine volcaniclastic rocks. *Geol. Soc. Lond. Spec. Publ.*, **16**, 5–27.

Fouquet, Y. (1999) Where are the large hydrothermal sulphide deposits in the oceans? In: *Mid-Ocean Ridges: Dynamics of Processes Associated with Creation of New Ocean Crust* (Eds Cann, J.R., Elderfield, H. and Laughton, A.), pp. 211–224. Cambridge University Press, Cambridae.

Garcia-Fresca, B., **Pinkston, D.**, **Loucks, R.G.** and **LeFever, R.** (2018) The three forks playa lake depositional model: implications for characterization and development of an unconventional carbonate play. *AAPG Bull.*, **102**, 1455–1488.

Genna, D., **Gaboury, D.** and **Roy, G.** (2014) Evolution of a volcanogenic hydrothermal system recorded by the behavior of LREE and Eu: case study of the key Tuffite at Bracemac–McLeod deposits, Matagami, Canada. *Ore Geol. Rev.*, **63**, 160–177.

Geske, A., **Goldstein, R.H.**, **Mavromatis, V.**, **Richter, D.K.**, **Buhl, D.**, **Kluge, T.**, **John, C.M.** and **Immenhauser, A.** (2015a) The magnesium isotope (δ^{26}Mg) signature of dolomites. *Geochim. Cosmochim. Acta*, **149**, 131–151.

Geske, A., **Lokier, S.**, **Dietzel, M.**, **Richter, D.K.**, **Buhl, D.** and **Immenhauser, A.** (2015b) Magnesium isotope composition of sabkha porewater and related (sub-) recent stoichiometric dolomites, Abu Dhabi (UAE). *Chem. Geol.*, **393-394**, 112–124.

Gill, R. (2010) *Igneous Rocks and Processes*. Wiley-Blackwell, Malaysia.

Graf, D.L. and **Goldsmith, J.R.** (1956) Some hydrothermal syntheses of dolomite and protodolomite. *J. Geol.*, **64**, 173–186.

Gregg, J.M., **Bish, D.L.**, **Kaczmarek, S.E.** and **Machel, H.G.** (2015) Mineralogy, nucleation and growth of dolomite in the laboratory and sedimentary environment: a review. *Sedimentology*, **62**, 1749–1769.

Gromet, L.P., **Haskin, L.A.**, **Korotev, R.L.** and **Dymek, R.F.** (1984) The “north American shale composite”: its compilation, major and trace element characteristics. *Geochim. Cosmochim. Acta*, **48**, 2469–2482.

Gu, L., **Hu, S.**, **Yu, C.**, **Wu, C.** and **Yan, Z.** (2001) Initiation and evolution of the Bogda subduction-toyn-tupe rift. *Acta Petrol. Sin.*, **17**, 585–597 (in Chinese).

Guo, P., **Wen, H.**, **Gibert, L.**, **Jin, J.**, **Wang, J.** and **Lei, H.** (2021) Deposition and diagenesis of the early Permian volcanic-related alkaline playa-lake dolomitic shales, NW Junggar Basin, NW China. *Mar. Petrol. Geol.*, **123**, 104780.

Gupta, A.K. and **Fyfe, W.S.** (1975) Leucite survival: the alteration to analcime. *Can. Mineral.*, **13**, 361–363.

Hackley, P., **Fishman, N.**, **Wu, T.** and **Baugher, G.** (2016) Organic petrology and geochemistry of mudrocks from the lacustrine Lucaogou formation, Santanghu Basin, Northwest China: application to lake basin evolution. *Int. J. Coal Geol.*, **168**, 20–34.

Hammond, A.P., **Carroll, A.R.**, **Smith, M.E.** and **Lowenstein, T.K.** (2019) Bicarbonate rivers: connecting Eocene magmatism to the world’s largest Na-carbonate evaporite. *Geology*, **47**, 1020–1024.

Hay, R.L., **Guldman, S.G.**, **Matthews, J.C.**, **Lander, R.H.**, **Duffin, M.E.** and **Kyser, T.K.** (1991) Clay mineral diagenesis in core KM-3 of Searles Lake, California. *Clays Clay Miner.*, **39**, 84–96.

Hips, K., **Haas, J.**, **Poros, Z.**, **Kele, S.** and **Budai, T.** (2015) Dolomitization of Triassic microbial mat deposits (Hungary): origin of microcrystalline dolomite. *Sed. Geol.*, **318**, 113–129.

Holland, H.D. and **Zimmermann, H.** (2000) The dolomite problem revisited. *Int. Geol. Rev.*, **42**, 481–490.

Hollis, C., **Bastesen, E.**, **Boyce, A.**, **Corlett, H.**, **Gawthorpe, R.**, **Hirani, J.**, **Rotevatn, A.** and **Whitaker, F.** (2017) Fault-controlled dolomitization in a Rift Basin. *Geology*, **45**, 219–222.

Hood, A.S., **Wallace, M.W.** and **Drysdale, R.N.** (2011) Neoproterozoic aragonite-dolomite seas? Widespread marine dolomite precipitation in Cryogenian reef complexes. *Geology*, **39**, 871–874.

Huang, K.-J., **Shen, B.**, **Lang, X.-G.**, **Tang, W.-B.**, **Peng, Y.**, **Ke, S.**, **Kaufman, A.J.**, **Ma, H.-R.** and **Li, F.-B.** (2015) Magnesium isotopic compositions of the Mesoproterozoic dolostones: implications for mg isotopic systematics of marine carbonates. *Geochim. Cosmochim. Acta*, **164**, 333–351.

Ilich, M. (1974) Hydrothermal-sedimentary dolomite: the missing link? *AAPG Bull.*, **58**, 1331–1347.

Jiang, Y., **Zhao, S.**, **Ma, C.** and **Zhang, J.** (2008) Characteristics of rock-forming minerals of analcime phonolite in the Damxung area, Qinghai-Tibet plateau: evidence for primary analcime. *Earth Sci.*, **33**, 320–327 (in Chinese).

Jiao, X., **Liu, Y.**, **Yang, W.**, **Zhou, D.**, **Bai, B.**, **Zhang, T.**, **Zhao, M.**, **Li, Z.**, **Meng, Z.**, **Yang, Y.** and **Li, Z.** (2020) Fine-grained volcanic-hydrothermal sedimentary rocks in Permian Lucaogou formation, Santanghu Basin, NW China: implications on hydrocarbon source rocks and accumulation in lacustrine rift basins. *Mar. Petrol. Geol.*, **114**, 104201.

Jiao, X., **Liu, Y.**, **Yang, W.**, **Zhou, D.**, **Li, H.** and **Jin, M.** (2018a) A magmatic-hydrothermal lacustrine exhalite from the Permian Lucaogou formation, Santanghu Basin, NW China-the volcanogenic origin of fine-grained clastic sedimentary rocks. *J. Asian Earth Sci.*, **156**, 11–25.

Jiao, X., **Liu, Y.**, **Yang, W.**, **Zhou, D.**, **Wang, S.**, **Jin, M.**, **Sun, B.** and **Fan, T.** (2018b) Mixed biogenic and hydrothermal quartz in Permian lacustrine shale of Santanghu Basin, NW China-implications for penecontemporaneous transformation of silica minerals. *Int. J. Earth Sci.*, **107**, 1989–2009.

Jones, B. and **Manning, D.A.C.** (1994) Comparison of geochemical indices used for the interpretation of palaeoredox conditions in ancient mudstones. *Chem. Geol.*, **111**, 111–129.

Kele, S., **Demeny, A.**, **Siklosy, Z.**, **Nemeth, T.**, **Toth, M.** and **Kovacs, M.B.** (2008) Chemical and stable isotope composition of recent hot-water travertines and associated thermal waters, from Egerszalok, Hungary: depositional facies and non-equilibrium fractionation. *Sed. Geol.*, **211**, 53–72.

Kelley, D.S., **Karson, J.A.**, **Blackman, D.K.**, **Früh-Green, G.L.**, **Butterfield, D.A.**, **Lilley, M.D.**, **Olson, E.J.**, **Schrenk, M.O.**, **Roe, K.R.**, **Lebon, G.T.**, **Rivizzigno, P.** and **the AT3-60 Shipboard Party** (2001) An off-axis hydrothermal vent field near the mid-Atlantic ridge at 30°N. *Nature*, **412**, 145–149.

Kelley, D.S., **Karson, J.A.**, **Früh-Green, G.L.**, **Yoerger, D.R.**, **Shank, T.M.**, **Butterfield, D.A.**, **Hayes, J.M.**, **Schrenk, M.O.**, **Olson, E.J.**, **Proskurowski, G.**, **Jakuba, M.**, **Bradley, A.**, **Larson, B.**, **Ludwig, K.**, **Glickson, D.**, **Buckman, K.**, **Bradley, A.S.**, **Brazelton, W.J.**, **Roe, K.**, **Elend, M.J.**, **Delacour, A.**, **Bernasconi, S.M.**, **Lilley, M.D.**, **Baross, J.A.**,

Summons, R.E. and **Sylva, S.P.** (2005) A serpentinite-hosted submarine ecosystem: the lost City hydrothermal field. *Science*, **307**, 1428–1434.

Kenward, P.A., **Goldstein, R.H.**, **Gonzalez, L.A.** and **Roberts, J.A.** (2009) Precipitation of low-temperature dolomite from an anaerobic microbial consortium: the role of methanogenic archaea. *Geobiology*, **7**, 556–565.

Koeshidayatullah, A., **Corlett, H.**, **Stacey, J.**, **Swart, P.K.**, **Boyce, A.** and **Hollis, C.** (2020) Origin and evolution of fault-controlled hydrothermal dolomitization fronts: a new insight. *Earth Planet. Sci. Lett.*, **541**, 116291.

Land, L.S. (1998) Failure to precipitate dolomite at 25°C from dilute solution despite 1000-fold oversaturation after32 years. *Aquat. Geochem.*, **4**, 361–368.

Last, W.M. (1990) Lacustrine dolomite–an overview of modern, Holocene, and Pleistocene occurrences. *Earth-Sci. Rev.*, **27**, 221–263.

Lawrence, M.G. and **Kamber, B.S.** (2006) The behaviour of the rare earth elements during estuarine mixing-revisited. *Mar. Chem.*, **100**, 147–161.

Li, H., **Liu, Y.**, **Yang, K.**, **Liu, Y.** and **Niu, Y.** (2021) Hydrothermal mineral assemblages of calcite and dolomite-analcime-pyrite in Permian lacustrine Lucaogou mudstones, eastern Junggar Basin, Northwest China. *Mineral. Petrol.*, **115**, 63–85.

Lilley, M.D., **Butterfield, D.A.**, **Lupton, J.E.** and **Olson, E.J.** (2003) Magmatic events can produce rapid changes in hydrothermal vent chemistry. *Nature*, **422**, 878–881.

Liu, Y., **Jiao, X.**, **Li, H.**, **Yuan, M.**, **Yang, W.**, **Zhou, X.**, **Liang, H.**, **Zhou, D.**, **Zheng, C.**, **Sun, Q.** and **Wang, S.** (2012) Mantle exhalative hydrothermal original dolostones of Permian, in Yuejingou section, Santanghu area, Xinjiang province. *Sci. China Earth Sci.*, **55**, 183–192.

Liu, B., **Song, Y.**, **Zhu, K.**, **Su, P.**, **Ye, X.** and **Zhao, W.** (2020) Mineralogy and element geochemistry of salinized lacustrine organic-rich shale in the middle Permian Santanghu Basin: implications for paleoenvironment, provenance, tectonic setting and shale oil potential. *Mar. Petrol. Geol.*, **120**, 104569.

Liu, C.L., **Zhao, Q.H.** and **Wang, P.X.** (2001) Correlation between carbon and oxygen isotopic ratios of lacustrine carbonates and types of oil-producing paleolakes. *Geochimica*, **30**, 363–367 (in Chinese with English abstract).

Lonnee, J. and **Machel, H.G.** (2006) Pervasive dolomitization with subsequent hydrothermal alteration in the Clarke Lake gas field, middle Devonian slave point formation, British Columbia, Canada. *AAPG*, **90**, 1739–1761.

Lowenstein, T.K., **Jagniecki, E.A.**, **Carroll, A.R.**, **Smith, M.E.**, **Renaut, R.W.** and **Owen, R.B.** (2017) The Green River salt mystery: what was the source of the hyperalkaline lake waters? *Earth-Sci. Rev.*, **173**, 295–306.

Mazzullo, S.J. (2000) Organogenic dolomitization in peritidal to deep-sea sediments. *J. Sediment. Res.*, **70**, 10–23.

Möller, P. and **Bau, M.** (1993) Rare-earth patterns with positive cerium anomaly in alkaline waters from Lake Van, Turkey. *Earth Planet. Sci. Lett.*, **117**, 671–676.

Nan, Y., **Liu, Y.**, **Zhou, D.**, **Zhou, N.**, **Jiao, X.** and **Zhou, P.** (2016) Characteristics and origin of amygdale and crack fillers in volcanic rock of late carboniferous in the Santanghu Basin, Xinjiang. *Acta Petrol. Sinica*, **32**, 1901–1913 (in Chinese).

Newell, D.L., **Jensen, J.L.**, **Frantz, C.M.** and **Vanden Berg, M.D.** (2017) Great salt Lake (Utah) microbialite δ^{13}C, δ^{18}O, and δ^{15}N record fluctuations in lake biogeochemistry since the late Pleistocene. *Geochem. Geophys. Geosyst.*, **18**, 3631–3645.

Palmer, M.R. and **Elderfield, H.** (1985) Sr isotope composition of sea water over the past 75 Myr. *Nature*, **314**, 526–528.

Pan, Y., **Huang, Z.**, **Li, T.**, **Guo, X.**, **Xu, X.** and **Chen, X.** (2020) Environmental response to volcanic activity and its effect on organic matter enrichment in the Permian Lucaogou formation of the Malang sag, Santanghu Basin, Northwest China. *Palaeogeogr. Palaeoclimatol. Palaeoecol.*, **560**, 110024.

Pecoraino, G., **D'Alessandro, W.** and **Inguaggiato, S.** (2015) The other side of the coin: geochemistry of Alkaline Lakes in volcanic areas. In: *Volcanic Lakes* (Eds Rouwet, D., Christenson, B., Tassi, F. and Vandemeulebrouck, J.), pp. 219–237. Springer, Berlin, Heidelberg.

Petrash, D.A., **Bialik, O.M.**, **Bontognali, T.R.R.**, **Vasconcelos, C.**, **Roberts, J.A.**, **McKenzie, J.A.** and **Konhauser, K.O.** (2017) Microbially catalyzed dolomite formation: from near-surface to burial. *Earth-Sci. Rev.*, **171**, 558–582.

Pittari, A., **Muir, S.L.** and **Hendy, C.H.** (2016) Lake-floor sediment texture and composition of a hydrothermally-active, volcanic Lake, Lake Rotomahana. *J. Volcanol. Geotherm. Res.*, **314**, 169–181.

Procesi, M., **Ciotoli, G.**, **Mazzini, A.** and **Etiope, G.** (2019) Sediment-hosted geothermal systems: review and first global mapping. *Earth-Sci. Rev.*, **192**, 529–544.

Roberts, J.A., **Bennett, P.C.**, **Gonzalez, L.A.**, **Macpherson, G.L.** and **Milliken, K.L.** (2004) Microbial precipitation of dolomite in methanogenic groundwater. *Geology*, **32**, 277–280.

Rothschild, L.J. and **Mancinelli, R.L.** (2001) Life in extreme environments. *Nature*, **409**, 1092–1101.

Roux, J. and **Hamilton, D.L.** (1976) Primary igneous analcite-an experimental study. *J. Petrol.*, **17**, 244–257.

Sanz-Montero, M.E., **Rodríguez-Aranda, J.P.** and **García Del Cura, M.A.A.** (2008) Dolomite-silica stromatolites in Miocene lacustrine deposits from the Duero Basin, Spain: the role of organotemplates in the precipitation of dolomite. *Sedimentology*, **55**, 729–750.

Schumacher, R. and **Schmincke, H.U.** (1995) Models for the origin of accretionary lapilli. *Bull. Volcanol.*, **56**, 626–639.

Sibley, D.F. and **Gregg, J.M.** (1987) Classification of dolomite rock textures. *J. Sediment. Res.*, **57**, 967–975.

Smith, L.B., Jr. (2006) Origin and reservoir characteristics of upper Ordovician Trenton-Black River hydrothermal dolomite reservoirs in New York. *AAPG*, **90**, 1691–1718.

Song, D., **He, D.** and **Wang, S.** (2013) Source rock potential and organic geochemistry of carboniferous source rocks in Santanghu Basin, NW China. *J. Earth Sci.*, **24**, 355–370.

Southgate, P.N., **Lambert, I.B.**, **Donnelly, T.H.**, **Henry, R.**, **Etminan, H.** and **Weste, G.** (1989) Depositional environments and diagenesis in lake parakeelya: a Cambrian alkaline playa from the officer basin, South Australia. *Sedimentology*, **36**, 1091–1112.

Stamatakis, M.G. (1989) Authigenic silicates and silica polymorphs in the Miocene saline-alkaline deposits of the Karlovassi Basin, Samos, Greece. *Econ. Geol.*, **84**, 788–798.

Stüeken, E.E., **Buick, R.** and **Schauer, A.J.** (2015) Nitrogen isotope evidence for alkaline lakes on late Archean continents. *Earth Planet Sci. Lett.*, **411**, 1–10.

Sun, S.S. and **McDonough, W.F.** (1989) Chemical and isotopic systematics of oceanic basalts: implications for mantle composition and processes. *Geol. Soc. Lond. Spec. Publ.*, **42**, 313–345.

Talbot, M.R. and **Kelts, K.** (1990) Paleolimnological signatures from carbon and oxygen isotopic ratios in carbonates from organic carbon-rich lacustrine sediments. *AAPG Mem.*, **50**, 99–112.

Teng, Z. (2017) Magnesium isotope geochemistry. *Rev. Mineral. Geochem.*, **82**, 219–287.

Vasconcelos, C. and **McKenzie, J.A.** (1997) Microbial mediation of modern dolomite precipitation and diagenesis under anoxic conditions (Lagoa Vermelha, Rio de Janeiro, Brazil). *J. Sediment. Res.*, **67**, 378–390.

Wacey, D., **Wright, D.T.** and **Boyce, A.J.** (2007) A stable isotope study of microbial dolomite formation in the Coorong region, South Australia. *Chem. Geol.*, **244**, 155–174.

Wang, S., **Liu, Y.**, **Zhang, H.**, **Zhou, D.**, **Jiao, X.** and **Nan, Y.** (2015) Geochemical characteristics and tectonic setting of the middle Permian Tiaohu formation mafic-ultramafic rocks of Santanghu area, Xinjiang, Northwest China. *Sci. China Earth Sci.*, **58**, 1924–1938.

Warren, J. (2000) Dolomite: occurrence, evolution and economically important associations. *Earth Sci. Rev.*, **52**, 1–81.

Warthmann, R., **van Lith, Y.**, **Vasconcelos, C.G.**, **McKenzie, J.A.** and **Karpoff, A.M.** (2000) Bacterially induced dolomite precipitation in anoxic culture experiments. *Geology*, **28**, 1091–1094.

Wen, H., **Zheng, R.**, **Qing, H.**, **Fan, M.**, **Li, Y.** and **Gong, B.** (2013) Primary dolostone related to the cretaceous lacustrine hydrothermal sedimentation in Qingxi sag, Jiuquan Basin on the northern Tibetan plateau. *Sci. China Earth Sci.*, **56**, 2080–2093.

White, J.D.L. (2000) Subaqueous eruption-fed density currents and their deposits. *Precambrian Res.*, **101**, 87–109.

Wilkinson, J.F.G. (1977) Analcime phenocrysts in a vitrophyric analcimite-primary or secondary? *Contrib. Mineral. Petrol.*, **64**, 1–10.

Xia, L., **Xia, Z.**, **Xu, X.**, **Li, X.** and **Ma, Z.** (2008) Petrogenesis of carboniferous-early Permian rift-related volcanic rocks in the Tianshan and its neighboring areas, Northwestern China. *Northwestern Geol.*, **41**, 1–68 (in Chinese).

Xie, S., **Pancost, D.R.**, **Wang, Y.**, **Yang, H.**, **Wignall, B.P.**, **Luo, G.**, **Jia, C.** and **Chen, L.** (2010) Cyanobacterial blooms tied to volcanism during the 5 m.y. Permo-Triassic biotic crisis. *Geology*, **38**, 447–450.

Yang, W., **Feng, Q.**, **Liu, Y.**, **Tabor, N.**, **Miggins, D.**, **Crowley, J.L.**, **Lin, J.** and **Thomas, S.** (2010) Depositional environments and cyclo- and chronostratigraphy of uppermost carboniferous-lower Triassic fluvial-lacustrine deposits, southern Bogda Mountains, NW China-a terrestrial paleoclimatic record of mid-latitude NE Pangea. *Glob. Planet. Change*, **73**, 15–113.

Yang, Z., **Whitaker, F.F.**, **Liu, R.**, **Phillips, J.C.** and **Zhong, D.** (2021) A new model for formation of lacustrine primary dolomite by subaqueous hydrothermal venting. *Geophys. Res. Lett.*, **48**, e2020GL091335.

Yang, Z., **Zhong, D.**, **Whitaker, F.**, **Lu, Z.**, **Zhang, S.**, **Tang, Z.**, **Liu, R.** and **Li, Z.** (2020) Syn-sedimentary hydrothermal dolomites in a lacustrine rift basin: petrographic and geochemical evidence from the lower cretaceous Erlian Basin, Northern China. *Sedimentology*, **67**, 305–329.

Yu, K., **Cao, Y.**, **Qiu, L.**, **Sun, P.**, **Jia, X.** and **Wan, M.** (2018) Geochemical characteristics and origin of sodium carbonates in a closed alkaline basin: the lower Permian Fengcheng formation in the Mahu sag, northwestern Junggar Basin, China. *Palaeogeogr. Palaeoclimatol. Palaeoecol.*, **511**, 506–531.

Zhang, R., **Jiang, T.**, **Tian, Y.**, **Xie, S.**, **Zhou, L.**, **Li, Q.** and **Jiao, N.** (2017) Volcanic ash stimulates growth of marine autotrophic and heterotrophic microorganisms. *Geology*, **45**, 679–682.

Zhang, S., **Liu, C.**, **Liang, H.**, **Jia, L.**, **Bai, J.**, **Zhang, L.** and **Wang, J.** (2021) Mineralogical composition and organic matter characteristics of lacustrine fine-grained volcanic-hydrothermal sedimentary rocks: a data-driven analytics for the second member of Permian Lucaogou formation, Santanghu Basin, NW China. *Mar. Petrol. Geol.*, **126**, 104920.

Zhao, Z., **Guo, Z.** and **Han, B.** (2006) The geochemical characteristic and tectonic-magmatic implications of the late-Paleozoic volcanic rocks from Santanghu basin, eastern Xinjiang, Northwest China. *Acta Petrol. Sin.*, **22**, 199–214.

Zheng, R., **Wen, H.**, **Fan, M.**, **Wang, M.**, **Wu, G.** and **Xia, P.** (2006) Lithological characteristics of sublacustrine white smoke type exhalative rock of the Xiagou formation in Jiuxi Basin. *Acta Petrol. Sin.*, **22**, 3027–3038 (in Chinese).

Zhou, D., **Liu, Y.**, **Xing, X.**, **Hao, J.**, **Dong, Y.** and **Ouyang, Z.** (2006) The paleotectonic setting reverting and regional tectonic setting tracking of basalt during Permian in Tu-ha, Santanghu basin in Xinjiang. *Sci. China Ser. D Earth Sci.*, **36**, 143–153 (in Chinese).

Manuscript received 31 December 2021; revision accepted 25 July 2022

Supporting Information

Additional information may be found in the online version of this article:

Table S1. Chemical compositions of dolomite crystals in the Lucaogou Formation in Santanghu Basin.

Table S2. Trace and rare earth elemental compositions (ppm) of three types dolostones from the Lucaogou Formation in Santanghu Basin.

Figure S1. Stratigraphic chart of Carboniferous–Jurassic deposits in Santanghu Basin (modified after Jiao *et al.*, 2020).

Figure S2. Seismic sections and line drawings of two sizes of cone-shaped stratigraphic build-ups in the Santanghu Basin. The cones have a flat base and internal reflections sloping away from an apex. The reflections in the upper parts of the cones are continuous with high amplitude, whereas those in the lower parts are chaotic. The geometry and internal pattern suggest that the cones are positive aggradational buildups. Individual buildups interfinger with each other to form a variety of offlap, onlap, downlap, parallel and truncational termination patterns, indicating multiple periods of up-building. Two types of buildups are present based on their size and duration. The first type is large, ranging from 1 to 6 km wide and 100 to 500 m high, and extends from the Haerjiawu and Lucaogou formations to the Tiaohu Formation. (A) and (B) Lithofacies of wells in this build-up are mainly tuff, tuffaceous shale and igneous rocks. Hence, this type of build-up was interpreted as the volcanic dominated deposit centre (volcanic centre). The second type is small, ranging from hundreds of metres wide and 10 to 200 m high, and occurs within the Lucaogou Formation. (C) and (D) The lithofacies are mainly interlaminated tuffaceous shale and dolostones. This type is interpreted as sub-volcanic–hydrothermal deposit centre. A total of eight large buildups accumulated at the centre part of Malang Depression and 32 small buildups around the centre part are observed on seismic sections. Yellow lines are the formation boundaries. Green vertical lines are the location of wells. Vertical scales are estimated from synthetic seismograms. Red square is the location of Fig. S2C. Modified after Jiao *et al.* (2018b, 2020).

Figure S3. Photograph of vertical cut of cores showing the laminae (red arrows) of selected samples selected for micro-drilling. The sample numbers are marked at the lower right corner. Black scale bars are 1 cm.

Figure S4. (A) to (C) Lithostratigraphy of Lucaogou Formation and adjacent formations in wells N (depth from 2540 to 2855 m), L (3290 to 3790 m) and M (2650 to 3160 m). Lithofacies were mainly interpreted from well logs and calibrated using limited core observation. (D) Lithostratigraphy of core segments in (A) (marked with red bar) as established by core observation. Detailed sedimentary structures and boundary relationship are marked. Position of samples used in geochemical analysis is marked with N-2, L-1, M-1, *etc.* in (B), (C) and (D).

Figure S5. Fluid inclusions and their homogenization temperatures in dolomite crystals. Red scale bars are 1 μm.

Figure S6. Photomicrographs of non-dolomite minerals in dolostones. (A) Backscatter electron microprobe image showing a recrystallized dolomite-filled fluid escape structures (above white dashed lines). The rest of the photograph is composed mainly of microcrystal dolomite. This feature suggests pore fluid originated from the lower part and caused recrystallization of dolomite. White grains are pyrite and are concentrated in the fluid escape structure. Sample N-3. (B) A close-up of the white-dashed box in (A), showing that recrystallized dolomite crystals (bright grey) are euhedral, and some are replaced by magnesite (dark grey), indicating local Mg-rich fluid. (C) SEM image showing a shard-like quartz grain (red arrow) in the intercrystalline pore of dolomite (dark grey). Sample N-3. (D) A quartz grain in dolostone with a typical hexagonal columnar shape with a pinnacle (yellow arrow) on one side and a smooth concave–convex fracture on the other side (red arrow). The surfaces are smooth without scratches and pits, indicating little rounding and transport. Sample N-5. (E) A fracture (outlined by white dashed lines) in dolostone filled by autogenetic and euhedral quartz crystals. Sample N-5. (F) Backscatter electron microprobe image of a shard-like analcite grain (red arrow) in a dolomite (bright grey) dominated background, indicating that some vitric grains were altered to analcite. Dark grey angular grains are plagioclase. Sample M-1. (G) Backscatter electron microprobe image of clay-sized analcite (dark grey) serves as matrix and fills intercrystalline pore of dolomite (bright grey). Sample M-2. (H) A feldspar grain in dolostone with a smooth fracture (yellow arrow) and dissolution surface (red arrow). Sample L-3.

Figure S7. Scanning electron microscope (SEM) images showing microbial remains in types I and II dolostones. Red points are the EDS sites. (A) to (D) were observed on polished surfaces by argon ion, while (E) and (F) on fresh surface. (A) A possible microbial crust (dark grey) that is plurilocular and mainly composed of Ca and C. The bright grey background is microcrystalline dolomite. Microcrystalline dolomite crystals surround the crust and fill the cavities. Sample M-3. (B) An oval-shaped Fe-bearing dolomite in the cavity of the microbial crust. However, dolomite crystals outside the cavities contain no Fe. This suggests the different influence of microbial activities on dolomite nucleation. Sample M-3. (C) and (D) The same as (A), showing possible microbial crust (dark grey) in dolomite dominated background. Sample N-11. (E) Filamentary minerals that are 1 μm long and approximately hundreds of nm wide, irregularly curved, and intertwined to form a network, fill in the intercrystalline pore of dolomite showing intergrowth relationship with dolomite. Sample M-1. (F) A close up of the filamentary minerals. The EDS result shows their chemical compositions are Al and Si with possible Ca and Mg (may be contaminated from dolomite). Potassium, a main chemical composition for illite and mordenite, is not detected. Thus, the filamentary minerals are not illite or mordenite. Hence, the filamentary mineral is interpreted as partially mineralized microbial remains.